Cell

RNA damage compartmentalization by DHX9 stress granules

Graphical abstract

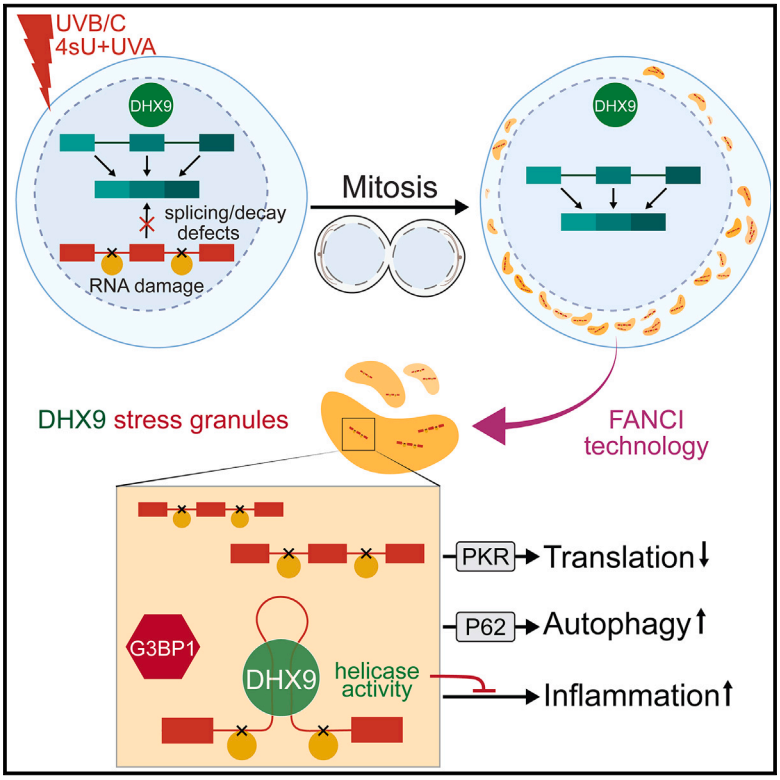

Highlights

- UV-induced RNA, but not DNA, crosslinking damage induces DHX9 SGs
- Cytoplasmic DHX9 SGs are enriched in damaged intron RNA
- DHX9 SGs activate multiple stress responses in daughter cells
- DHX9 SGs protect daughter cells from parental RNA damage

Authors

Yilong Zhou, Amol Panhale, Maria Shvedunova, ..., Gerhard Mittler, Thomas Manke, Asifa Akhtar

Correspondence

akhtar@ie-freiburg.mpg.de

In brief

Daughter cells arising from UV-exposed mother cells assemble stress granules that are marked by the dsRNA helicase DHX9. These stress granules sequester damaged intron RNA and activate several stress responses as a protective mechanism.

Zhou et al., 2024, Cell *187*, 1–18
March 28, 2024
https://doi.org/10.1016/j.cell.2024.02.028

CellPress

Cell

CellPress
OPEN ACCESS

Article

RNA damage compartmentalization by DHX9 stress granules

Yilong Zhou,[1] Amol Panhale,[1] Maria Shvedunova,[1] Mirela Balan,[1] Alejandro Gomez-Auli,[1] Herbert Holz,[1] Janine Seyfferth,[1] Martin Helmstädter,[4] Séverine Kayser,[4] Yuling Zhao,[1,2,3] Niyazi Umut Erdogdu,[1,2,3] Iga Grzadzielewska,[1,2,3] Gerhard Mittler,[1] Thomas Manke,[1] and Asifa Akhtar[1,5,*]

[1]Max Planck Institute of Immunobiology and Epigenetics, Freiburg, Germany
[2]Faculty of Biology, University of Freiburg, Freiburg, Germany
[3]International Max Planck Research School for Molecular and Cellular Biology (IMPRS-MCB), Freiburg, Germany
[4]EMcore, Renal Division, Department of Medicine, University Freiburg, Hospital Freiburg, University Faculty of Medicine, Freiburg, Germany
[5]Lead contact
*Correspondence: akhtar@ie-freiburg.mpg.de
https://doi.org/10.1016/j.cell.2024.02.028

SUMMARY

Biomolecules incur damage during stress conditions, and damage partitioning represents a vital survival strategy for cells. Here, we identified a distinct stress granule (SG), marked by dsRNA helicase DHX9, which compartmentalizes ultraviolet (UV)-induced RNA, but not DNA, damage. Our FANCI technology revealed that DHX9 SGs are enriched in damaged intron RNA, in contrast to classical SGs that are composed of mature mRNA. UV exposure causes RNA crosslinking damage, impedes intron splicing and decay, and triggers DHX9 SGs within daughter cells. DHX9 SGs promote cell survival and induce dsRNA-related immune response and translation shutdown, differentiating them from classical SGs that assemble downstream of translation arrest. DHX9 modulates dsRNA abundance in the DHX9 SGs and promotes cell viability. Autophagy receptor p62 is activated and important for DHX9 SG disassembly. Our findings establish non-canonical DHX9 SGs as a dedicated non-membrane-bound cytoplasmic compartment that safeguards daughter cells from parental RNA damage.

INTRODUCTION

There are three kinds of ultraviolet (UV) light in nature of which UVB (280–315 nm) and UVC (100–280 nm) cause DNA damage, including cyclobutane pyrimidine dimers (CPDs), pyrimidine 6-4 pyrimidone photoproducts (6-4PPs), and their Dewar isomers.[1–3] UVA radiation, on the other hand, is more than 1,000-fold less efficient at causing DNA damage because of its low photon energy.[4–6] While UV-induced DNA damage has been extensively studied over the last few decades,[1,5] early investigations identified UV-mediated RNA crosslinking damage in *Escherichia coli*,[7,8] suggesting that RNA species also possess the potential to accrue damage by UV.[9] In fact, UVB/C-catalyzed RNA-protein and RNA-RNA crosslinking reaction is widely used in crosslinking and immunoprecipitation (CLIP) experiments to explore RNA-protein and RNA-RNA interactions.[7,8,10–12] However, little is known about the consequence of UV-mediated RNA crosslinking damage in mammalian cells.

Stress granules (SGs) are ribonucleoprotein (RNP) condensates induced by various stress stimuli, including arsenite (As), heat shock (Hs), osmosis (Os), starvation, and UVC irradiation stresses.[13–15] They are microscopically visible cytoplasmic granules usually characterized by Ras GTPase-activating-protein-binding protein 1 (G3BP1) staining and have been proposed to preserve and stabilize mature mRNAs in the cytosol.[14,16] Based on the extensive studies of As- and Hs-induced SGs, it is believed that SGs are formed in response to translation repression and contain translation stalled mature mRNA.[14,17] However, it is unclear whether mature mRNA and mRNA-binding proteins represent the major components for all SG subtypes induced by different stress stimuli.[18,19]

In this study, we show that UV-induced RNA, but not DNA, crosslinking damage in mother cells triggers DHX9 SGs specifically in daughter cells. We uncovered that DHX9 SGs are non-canonical SGs enriched in intronic damaged RNA, unlike other types of SG, which are composed of mature mRNAs. Moreover, DHX9 SGs trigger a double-stranded RNA (dsRNA)-related immune response and translation shutdown in daughter cells, which is in striking contrast to classical SGs that assemble as a consequence of translation arrest rather than trigger it. We propose that the assembly of DHX9 SGs is a dedicated mechanism protecting daughter cells against parental RNA crosslinking damage.

RESULTS

UV-induced RNA, but not DNA, crosslinking damage triggers DHX9 SGs

Although at steady state, the dsRNA helicase DHX9 was restricted to the nucleus, we observed that a pool of DHX9 relocalized to cytoplasmic SGs during UVB and UVC irradiation, but

Please cite this article in press as: Zhou et al., RNA damage compartmentalization by DHX9 stress granules, Cell (2024), https://doi.org/10.1016/j.cell.2024.02.028

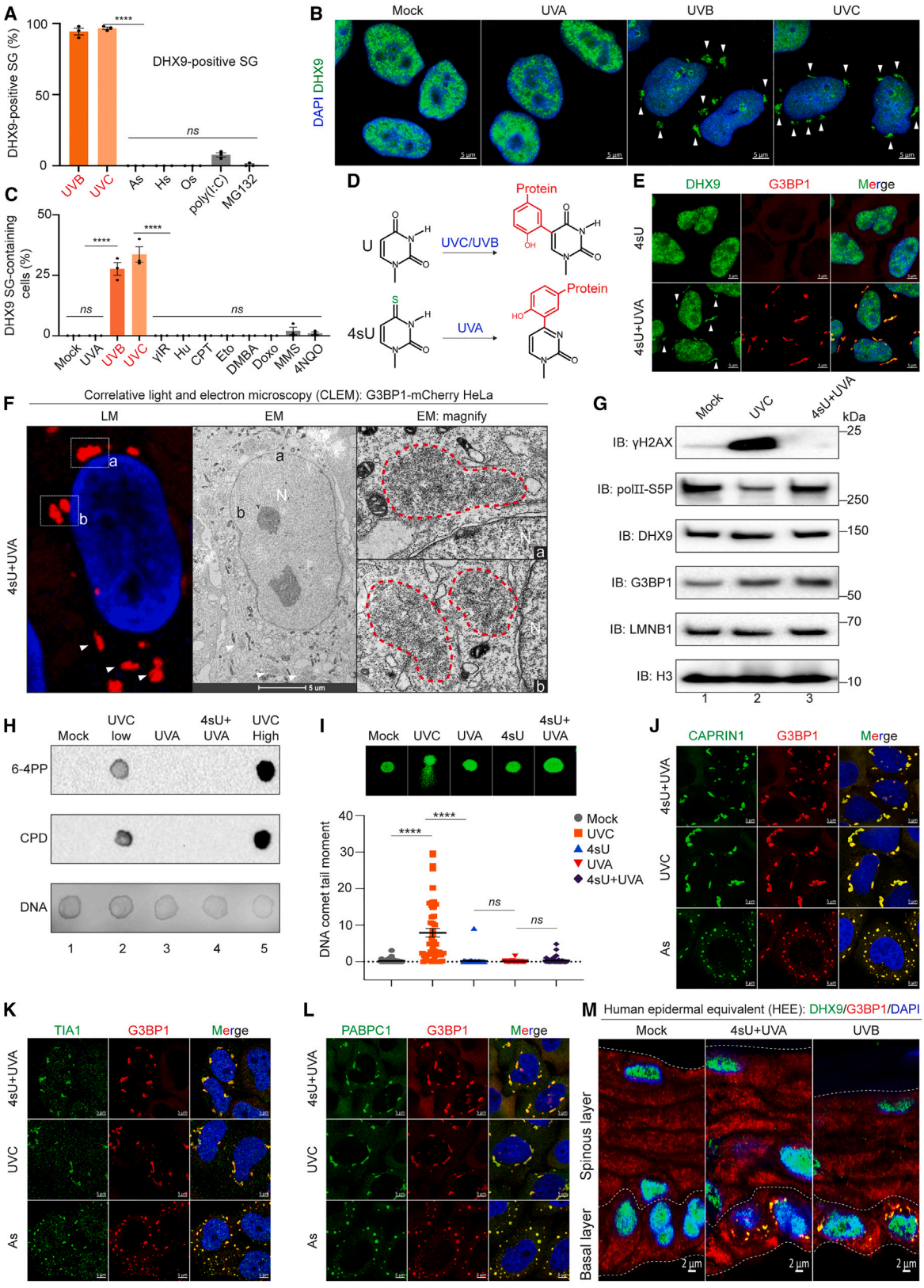

(legend on next page)

Please cite this article in press as: Zhou et al., RNA damage compartmentalization by DHX9 stress granules, Cell (2024), https://doi.org/10.1016/j.cell.2024.02.028

not following exposure to other stress stimuli (Figures 1A and S1A). We found that UVB and UVC, but not UVA, induced cytosolic DHX9 SGs (Figure 1B). However, none of the other DNA damage-inducing treatments we tested, such as γ irradiation, hydroxyurea, camptothecin, etoposide, 7,12-dimethylbenz[a] anthracene (DMBA), or doxorubicin, elicited the assembly of DHX9-positive SGs (Figures 1C and S1C). This result prompted us to question what was responsible for recruiting DHX9 to UVB- and UVC-induced SGs, since DNA damage alone was insufficient to do so.

Although less well characterized than their effect on DNA, UVB and UVC can also cause RNA damage by catalyzing crosslinks between RNA and proximal biomolecules. We therefore hypothesized that UVB- and UVC-induced RNA crosslinking damage could trigger the formation of DHX9-positive SGs. To be able to disentangle the effects of RNA and DNA damage, we took advantage of 4-thiouridine (4sU)—an analog of uridine, which can be incorporated into RNA but not into DNA, and selectively damaged by UVA—to produce RNA-protein and RNA-RNA crosslinking damage in cells (Figure 1D).[20] Cells treated with a low dose of UVA following 1 h of labeling with 4sU exhibited robust induction of DHX9 SGs visible under light and electron microscopes (Figures 1E, 1F, and S1B–S1D), with no detectable concomitant photoproducts, DNA strand breaks, or oxidative damage (Figures 1G–1I and S1E–S1G). Thus, RNA, but not DNA, damage is the molecular trigger for the formation of UV-induced DHX9-positive SGs, a specific subtype of SG that we henceforth refer to as "DHX9 SGs." Interestingly, treatment with RNA alkylation damage or oxidation damage inducers did not lead to DHX9 SG assembly, indicating that it is an RNA crosslinking damage-specific cellular response (Figure S2A). DHX9 SGs were formed in a UV-dose-dependent and 4sU time-course-dependent manner (Figures S2B–S2E; Video S1).

The DHX9 SGs contained proteins typical of SGs, including CAPRIN1, TIA1, PABPC1, TDP43, and STAU2 (Figures 1J–1L, S2F, and S2G). However, consistent with previous studies,[13,21] translation factor eIF3η, a marker of classical SGs, was much less enriched in 4sU + UVA- and UVC-induced DHX9 SGs than As-induced SGs (Figure S2H). Interestingly, G3BP1 and DHX9 proteins had distinct dynamics in the SGs. G3BP1 showed high mobility but DHX9 exhibited low mobility in Fluorescence Recovery after Photobleaching(FRAP) experiments and high resistance to 1,6-hexanediol treatment (Figures S2I–S2M; Video S2). We also observed the assembly of DHX9 SGs upon 4SU + UVA stress in three different keratinocyte cell lines (Figures S2N and S2O). Moreover, we established human epidermal equivalents (HEEs) and observed assembly of DHX9 SGs upon 4sU + UVA or UVB stresses, specifically in the basal layer where proliferating keratinocytes and melanocytes reside (Figures 1M, S3A, and S3B).

DHX9 SGs are enriched in damaged intron RNA

When we applied the recently published fractionation and antibody-based method to try to isolate SGs,[22] including DHX9 SGs, we discovered that their tight tethering to endoplasmic reticulum (ER) and nuclear membranes makes it difficult to pull these granules down efficiently (Figure S3C). This is in line with the recent work showing that ER membranes interact with As-induced SGs.[23] Inspired by the application of using flow cytometry technology to isolate other organelles,[24,25] we developed a method, fluorescence-activated non-membrane condensates isolation (FANCI), which utilizes flow cytometry sorting of fixed and sonicated cell lysates to purify SGs (Figure S3D). We successfully gated a population of G3BP1-mCherry^{high} particles in cell lysate from 4sU + UVA-treated cells but not in that from control or unfixed cells (Figures S3E and S3F). These purified particles were stable during downstream centrifugation and washing steps (Figure S3G). We could validate microscopically that the purified particles were intact SGs (Figure 2A). Furthermore, the DHX9 SGs purified by FANCI showed distinct localization patterns for DHX9 and G3BP1, which were similar to what we had observed in immunofluorescence experiments on intact cells (Figure S3H), indicating that the ultrastructure of the granules was preserved during isolation by FANCI.

We successfully utilized FANCI to isolate SGs induced by various stresses and confirmed that only 4sU + UVA-induced purified SGs contained DHX9 (Figures S3I–S3K). RNA sequencing (RNA-seq) further validated the high purity of FANCI-isolated SGs since there was little rRNA or mitochondrial RNA in purified SGs, compared with total RNA isolated from the cells (Figure S3L).

Figure 1. UV induces assembly of cytoplasmic DHX9 SGs

(A) The percentage of SGs that contain DHX9, mean ± SEM (n = 3 biological replicates from 3 independent experiments, >100 SGs were measured for each sample). Significance was scored by ordinary one-way ANOVA, ns: p>0.05,****p<0.0001.

(B) Representative confocal images of DHX9 and DAPI signal in HeLa cells 8 h after different UV treatments. White arrows mark DHX9 SGs. Scale bars, 5 μm.

(C) The percentage of cells that contain DHX9 SGs, mean ± SEM (n = 3 biological replicates from 3 independent experiments, >100 cells were measured for each sample). Significance was scored by ordinary one-way ANOVA, ns: p>0.05,****p<0.0001

(D) UV-induced RNA-protein crosslinking reaction. Red indicates the aromatic group of amino acids.

(E) Representative confocal images of DHX9 and G3BP1 signals in HeLa cells treated with 4sU + UVA. White arrows mark DHX9 SGs. Scale bars, 5 μm.

(F) Representative confocal image and correlative electron microscopy image of G3BP1-mCherry HeLa cells after 4sU + UVA treatment. White boxes mark the insets a and b, white arrows mark additional SGs located outside of the insets; red dotted lines in the insets indicate SGs; N, nucleus.

(G) Immunoblot of HeLa cells 8 h after treatment with UVC or 4sU + UVA. γH2AX: marker of DNA double-stranded breaks, RNA Pol II-S5P: marker of transcription.

(H) Total DNA dot blot of HeLa cells treated as indicated. UVC low: 5 mJ/cm^2; UVC high: 50 mJ/cm^2; 6-4PP, pyrimidine-pyrimidone (6-4) photoproduct; CPD, cyclobutane pyrimidine dimer.

(I) Representative images and quantitative analyses of DNA strand breaks by alkaline comet assay from HeLa cells treated as indicated. Significance was scored by ordinary one-way ANOVA, ns: p>0.05,****p<0.0001

(J–L) Representative confocal images of indicated protein and G3BP1 signals in HeLa cells treated with 4sU + UVA, UVC, or As. Scale bars, 5 μm.

(M) Representative confocal images of DHX9 and G3BP1 signals in cryosections of HEE 8 h after treatment with 4sU + UVA (100 mJ/cm^2) or UVB (100 mJ/cm^2). Scale bars, 2 μm.

See also Figures S1 and S2 and Videos S1 and S2.

Please cite this article in press as: Zhou et al., RNA damage compartmentalization by DHX9 stress granules, Cell (2024), https://doi.org/10.1016/j.cell.2024.02.028

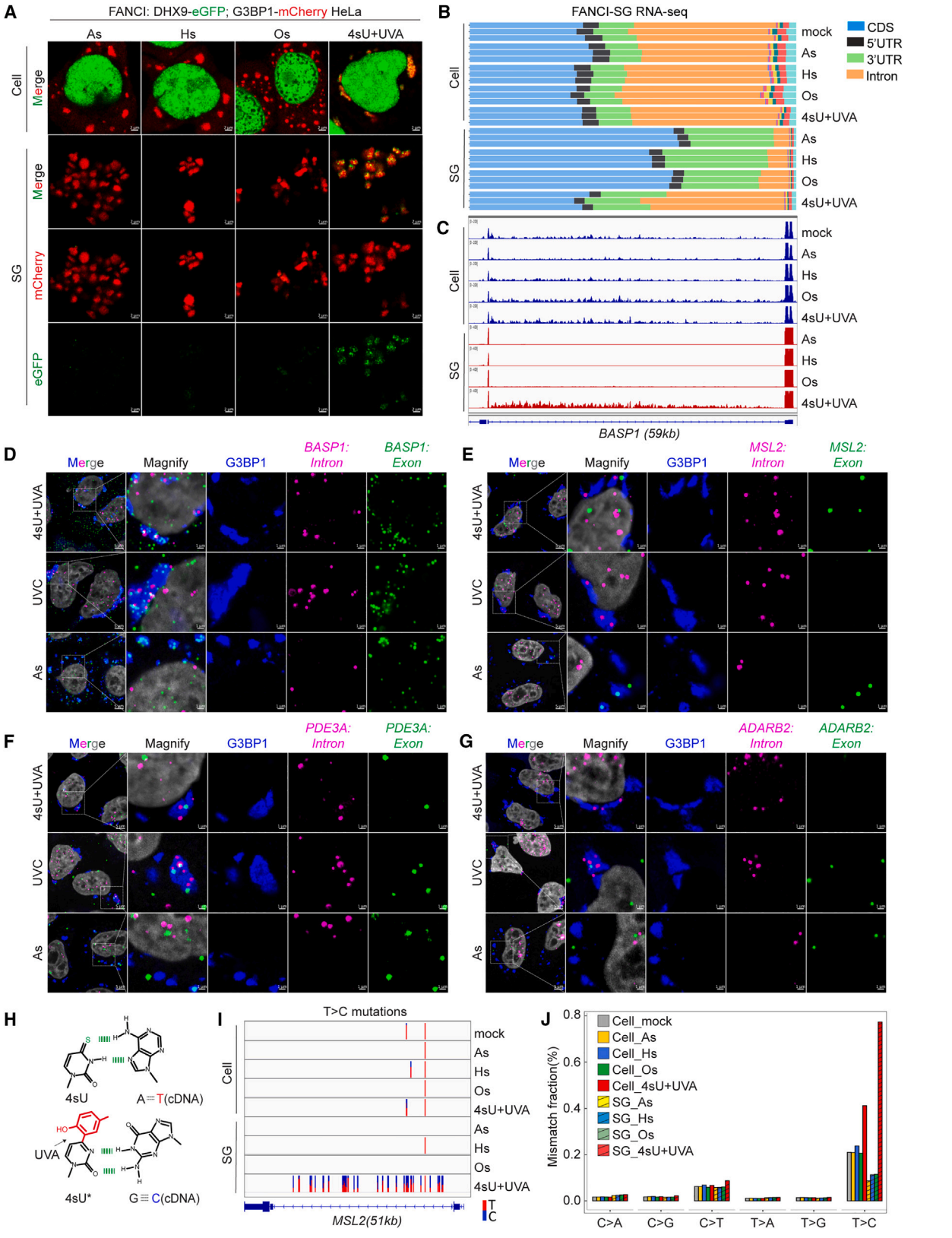

(legend on next page)

Please cite this article in press as: Zhou et al., RNA damage compartmentalization by DHX9 stress granules, Cell (2024), https://doi.org/10.1016/j.cell.2024.02.028

Surprisingly, RNA-seq analysis showed that while As-, Hs-, and Os-induced SGs were mainly composed of mature mRNA, there was a dramatic increase of intronic RNA in the DHX9 SGs induced by 4sU + UVA (Figures 2B, 2C, and S4A; Table S1). The transcripts showing intron enrichment in DHX9 SGs originate predominantly from long and AU-rich genes. In contrast, the lengths of the coding sequences (CDSs), 3′ untranslated regions (3′ UTR), and mature mRNAs of these genes are comparable to other genes expressed in the cell (Figure S4B). We also confirmed the observations from previous work that As-induced SGs are enriched in long mature mRNA (Figure S4C).[22]

We performed smRNA FISH experiments to validate the presence of introns in DHX9 SGs. As a negative control, we could show that neither *GAPDH* exon nor intron probes were enriched in 4sU + UVA- or As-induced SGs (Figure S4D). Interestingly, we could detect introns from five genes originally identified in our FANCI RNA-seq data (*BASP1*, *MSL2*, *PDE3A*, *ADARB2*, and *TRIO*) in 4sU + UVA and UVC-induced DHX9 SGs, but not in As-induced SGs, by smRNA FISH (Figures 2D–2G and S4E–S4G). Furthermore, we decided to take advantage of the fact that crosslinking damaged 4sU will be read as C upon reverse transcription in deep sequencing data to try to estimate the extent of RNA-protein crosslinking damage in our RNA-seq samples (Figure 2H). We found a dramatic increase of T>C mismatches in 4sU + UV-induced DHX9 SGs and could pinpoint most of these mismatches as mapping to introns. On the other hand, other types of mismatches are low and comparable between all samples (Figures 2I, 2J, and S4H–S4J). This indicates the sequestration of protein-crosslinking damaged intron RNA into DHX9 SGs.

UV-induced intron damage disturbs proper RNA processing

Intron crosslinking damage may impair splicing if it leads to the failure of pre-mRNA-binding proteins to disengage from pre-mRNAs, thereby blocking access by the spliceosome (Figure S5A). Indeed, splicing pattern analysis revealed an increase in abnormal splicing patterns of RNAs from the DHX9 SGs, compared with RNAs from other SGs or total expressed RNAs in the cell (Figure 3A). For example, sashimi plots revealed that while the *MSL2* and *EZH2* mRNAs from As-induced SGs were generated by proper splicing, their counterparts in DHX9 SGs frequently showed splicing at new sites in and even outside the gene locus (Figures 3B and S5B).

The crosslinking of proteins to intron RNA might impinge on exoribonuclease activity, leading to the persistence of damaged introns and pre-mRNAs in 4sU + UVA-treated cells.[26] We therefore analyzed RNA half-life time by treating the cells with flavopiridol, a general transcription inhibitor.[27] Although the intron abundance quickly decreased after transcription block in unirradiated cells, it remained high in cells subjected to RNA crosslinking damage, suggesting that introns were less sensitive to decay in 4sU + UVA-treated cells than untreated cells (Figures 3C–3E, S5C, and S5D; Table S1).

"Downstream of gene" (DOG) transcripts were shown as markers of nuclear RNA processing defects caused by osmotic stress and infection.[28–30] Consistently, we demonstrated that Os-induced, but not Hs-induced, SGs contained more DOGs, compared with As-induced SGs (Figures S5E and S5F). Notably, 4sU + UVA-induced DHX9 SGs contained an abundance of both upregulated and downregulated DOGs when compared with As-induced SGs, suggesting that 4sU + UVA indeed disrupts RNA processing (Figures S5G and S5H).

We then asked whether splicing inhibition could induce the formation of DHX9 SGs. Treatment with splicing inhibitor pladienolide B (PladB) triggered assembly of DHX9 SGs but to a lesser extent than 4sU + UVA stress (Figures 3F–3H). Surprisingly, although both UVC and PladB triggered cell death (Figure 3I), DHX9 SGs were exclusively observed in live cells and did not co-localize with or resemble micronuclei or apoptotic cells (Figures 3J and S5I–S5L). Moreover, inhibitors of RNA Pol II (but not RNA Pol I or RNA Pol III) prevented the formation of DHX9 SGs (Figures 3K and 3L), implicating damaged nascent mRNA rather than mature mRNA, rRNA, or tRNA in eliciting the assembly of DHX9 SGs. This is consistent with the finding that cells in which 4sU was washed out 3 h prior to UVA exposure failed to induce DHX9 SGs (Figure S2E). On the other hand, treatment with endoribonuclease RNase A or I, but not exoribonuclease RNase R, in permeabilized live cells eliminated DHX9 SGs, indicating that crosslinking damaged RNA is essential for DHX9 SG assembly (Figure 3M).

Intron damage triggers DHX9 SGs and activates a dsRNA-related stress response in daughter cells

Immunofluorescence staining showed that DHX9 SG-positive cells always came in pairs (Figure 4A), which are reminiscent of

Figure 2. SG purification and characterization by FANCI

(A) Representative confocal images of cells and FANCI-purified SGs from DHX9-eGFP; G3BP1-mCherry HeLa cells treated with the indicated stresses. Scale bars, 2 μm.

(B) Content of RNA isolated from HeLa cells and purified SGs. Intron, UTR, and CDS are highlighted. Each sample includes three biological replicates.

(C) Representative Integrative Genomics Viewer (IGV) snapshot showing RNA reads coverage on gene *BASP1* from indicated HeLa cells and SGs.

(D–G) Representative confocal images of G3BP1 and indicated gene exon and intron smRNA FISH staining in HeLa cells treated with the indicated stresses. White dashed line marks the magnified region.

(H) 4sU pairs with adenosine and is read as thymidine, but UVA-crosslinked 4sU pairs with guanosine in cDNA library preparation and is read as cytosine in RNA-seq.

(I) A representative gene locus (*MSL2*) showing the mismatch patterns (T>C) from the indicated samples. Sites of conversion of T to C in the RNA-seq are indicated with vertical red and blue bars where the proportion of blue and red indicates the proportion of reads exhibiting T>C conversion or lack of T>C conversion, respectively.

(J) Quantification of all types of mismatch in the indicated HeLa cells and purified SGs. The y axis depicts the percentage of indicated mismatches detected in RNA-seq data of the corresponding samples, calculated as the total number of indicated types of mismatched nucleotides relative to the total number of corresponding detected nucleotides.

See also Figures S3 and S4 and Table S1.

Please cite this article in press as: Zhou et al., RNA damage compartmentalization by DHX9 stress granules, Cell (2024), https://doi.org/10.1016/j.cell.2024.02.028

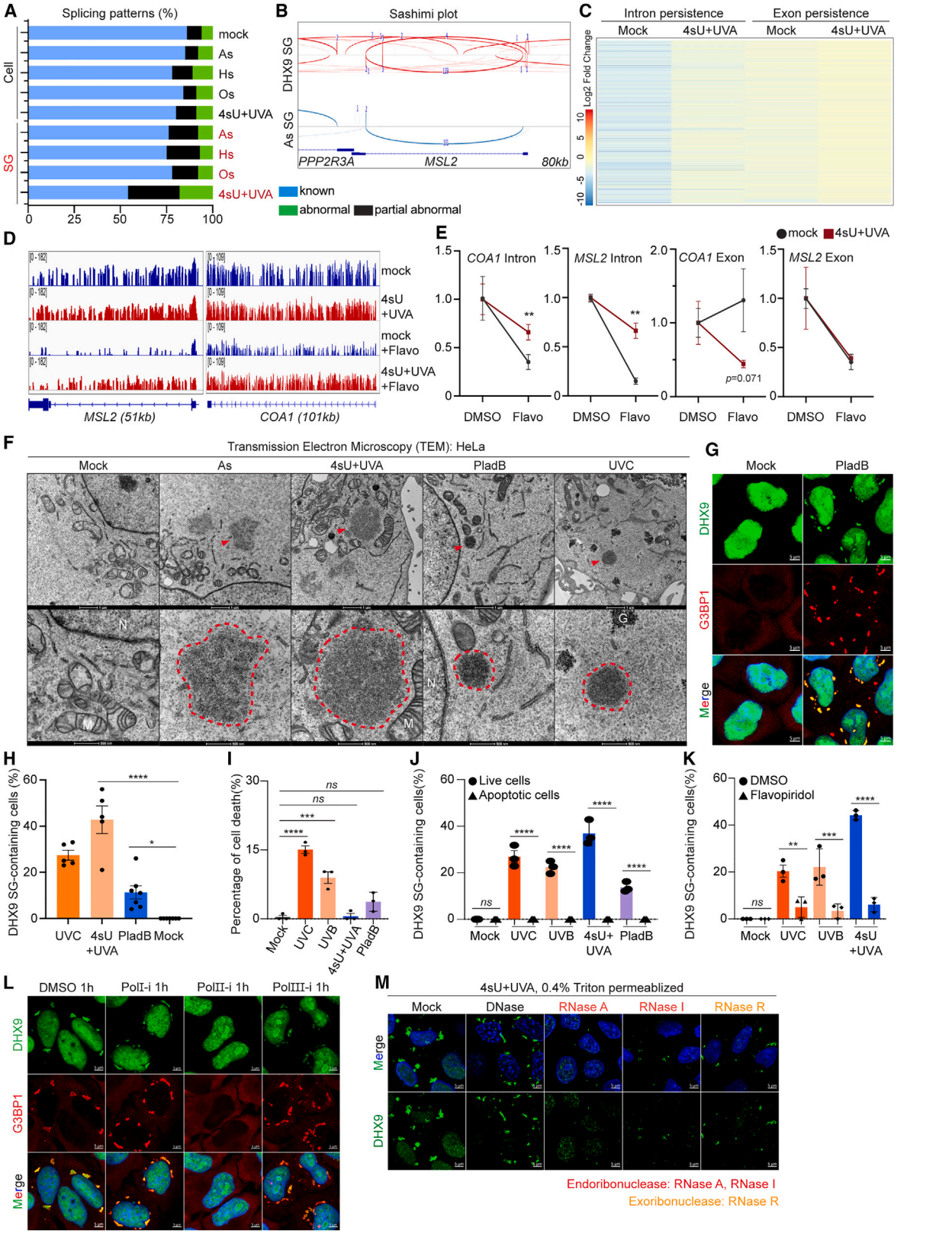

(legend on next page)

Please cite this article in press as: Zhou et al., RNA damage compartmentalization by DHX9 stress granules, Cell (2024), https://doi.org/10.1016/j.cell.2024.02.028

the pairs of daughter cells just separated after mitosis. Live-cell imaging indeed showed that the emergence of DHX9 SGs occurred exclusively in daughter cells that had recently undergone mitosis (Figure 4B; Video S3). Synchronization experiments suggested that damaged introns could persist for hours in cells but only trigger assembly of DHX9 SGs once the cells had undergone mitosis (Figure 4C). Moreover, live-cell imaging showed that once formed, DHX9 SGs remain in cells for about 30 h (Video S4). The majority (90%) of daughter cells containing DHX9 SGs failed to progress through the cell cycle. A fraction (<10%) still entered mitosis but only after DHX9 SGs were resolved (Figure S6A; Video S4).

We hypothesized that the disassembly of the nuclear envelope (NE) in mitosis, which releases nuclear contents to the cytoplasm, triggers the assembly of cytoplasmic DHX9 SGs. 1,6-Hexanediol is a small molecule widely used to reversibly disrupt nuclear pore complex integrity and induce nuclear content leakage.[32,33] We therefore incubated 4sU + UVA-treated cells with 1,6-hexanediol to mimic mitotic NE disassembly (Figure S6B). Live-cell imaging showed that while the bulk of DHX9 re-entered the nucleus after 1,6-hexanediol removal, a proportion of DHX9 formed G3BP1-positive granules in 4sU + UVA-treated cells without requiring them to have undergone mitosis (Figures 4D and S6C). Interestingly, smRNA FISH experiments demonstrated that these granules contained intron RNA (Figure S6D). Moreover, 1,6-hexanediol-mediated disruption of nuclear membrane integrity appeared to exacerbate the cytotoxic effect of damaged RNA (Figure S6E).

The assembly of SGs has been found to be coupled with translation shutdown in cells.[14] We therefore hypothesized that DHX9 SG-containing cells might be identifiable by their failure to incorporate the tyrosyl-tRNA-mimic antibiotic puromycin.[34] Indeed, cells that are negative for puromycin staining contained DHX9 SGs (Figure 4E), which indicated translation suppression in these cells. RNA-seq of fluorescence-activated cell sorting (FACS)-sorted puromycin-labeled cells (henceforth named Puro-seq) showed that the DHX9 SG-containing (puromycin^{low}) cells had a very different gene expression profile from cells lacking DHX9 SGs (puromycin^{high}), even though both underwent 4sU + UVA treatment (Figures 4F, S6F, and S6G; Table S1). Gene Ontology (GO) and gene set enrichment analysis (GSEA) showed that DHX9 SG-containing cells showed no upregulation of DNA damage response genes but specifically initiated dsRNA- and tumor necrosis factor (TNF)-related inflammatory gene expression (Figures 4G, S6H, and S6I). DHX9 SG-containing cells also lacked G2/M-stage gene expression but highly expressed G1-stage genes, compared with either DHX9 SG-lacking or unstressed cells (Figures 4G and S6I), which is consistent with our observation that only post-mitotic cells exhibit DHX9 SGs. We could validate these gene expression changes by quantitative reverse-transcription PCR (RT-qPCR) in HeLa and HaCAT cell lines (Figures 4H and S6J). We also observed increased immune gene expression in three different keratinocyte cell lines after 4sU + UVA treatment (Figure S6K). Moreover, nuclear translocation of p65 (nuclear factor [NF]-κB), a hallmark of inflammation, was detected specifically in DHX9 SG-containing keratinocytes in UV-stressed HEEs (Figure S6L).

Since the dsRNA stress response signature was detected, we wondered whether there was dsRNA accumulation in these cells. dsRNA (J2) staining revealed an accumulation of dsRNA specifically in UVC- and 4sU + UVA-induced but not As- or Hs-induced SGs (Figure 4I). In contrast, dsDNA staining displayed a dot-like pattern in the cytoplasm (corresponding to the labeling of the mitochondrial genome) but did not co-localize with DHX9 SGs, indicating that there was no dsDNA in the SGs (Figure S6M). Treatment with RNase A (non-specific) or RNase III (dsRNA-specific) eliminated the J2 staining in DHX9 SGs in fixed cells, confirming the J2 (dsRNA) staining specificity (Figures 4J and S6N). Moreover, we detected dsRNA in DHX9 SGs from two different keratinocyte cell lines upon 4sU + UVA treatment (Figure S6O). IR-*Alu* pairs in introns represent a major source of endogenous

Figure 3. UV-induced intron damage disturbs proper RNA processing

(A) Splicing junction analysis of RNA isolated from HeLa cells and SGs by RseQC. "Partial abnormal" represents splicing events engaging either an unannotated 5′ SS or 3′ SS; "abnormal" represents splicing junctions in which both 5′ SS and 3′ SS are unannotated.

(B) Sashimi plots showing the change of splicing pattern in *MSL2*. The curved line and number on it indicate the number of splicing reads.

(C) Heatmap showing changes in intron and exon levels in 4sU + UVA-stressed, flavopiridol-treated HeLa cells of genes showing intron enrichment in DHX9 SGs according to Table S1. Flavopiridol was added 2 h after 4sU + UVA at 10 μM for another 4 h.

(D) IGV snapshot of RNA-seq on *MSL2* and *COA1* genes from 4sU + UVA- and/or flavopiridol-treated samples as indicated. A log scale is applied to the IGV tracks.

(E) RT-qPCR assays quantifying changes in intron and exon levels in cells upon flavopiridol and 4sU + UVA treatments with intron- and exon-specific primers. Mean ± SEM (n = 3 technical replicates from a representative experiment out of 3 independent experiments). Significance was scored by unpaired t test with Welch's correction,**p<0.01

(F) Representative electron microscopy images of SGs in HeLa cells treated with the indicated stresses. Red dashed lines mark SGs. N, nucleus; M, mitochondria; G, glycogen granules.

(G–I) Representative confocal images (G) and quantification of DHX9 SG-positive cells (H) and dead cells (I) in HeLa cells treated with 4sU + UVA, splicing inhibitor PladB, or UVC, as indicated. Scale bars, 5 μm. Significance was scored by ordinary one-way ANOVA, ns: p>0.05, *p<0.05, ***p<0.001, ****p<0.0001

(J) Quantification of DHX9 SG-positive cells in live and dead cell populations after indicated treatments. Significance was scored by ordinary one-way ANOVA, ns: p>0.05, ****p<0.0001

(K and L) Quantification (K) and representative confocal images (L) of DHX9 and G3BP1 signals in HeLa cells treated with the indicated RNA polymerase inhibitors with or without 4sU together for 1 h, followed by administration of UVA or UVC stress. Samples were collected 8 h after UVA/UVC treatment. Significance was scored by ordinary one-way ANOVA, ns: p>0.05, **p<0.01, ****p<0.0001

(M) Representative cell images of DHX9-eGFP and DAPI signal in HeLa cells after 4sU + UVA treatment. The cells were permeabilized with 0.4% Triton X-100 for 10 min and treated with the indicated enzymes for 10 min.

See also Figure S5 and Table S1.

Please cite this article in press as: Zhou et al., RNA damage compartmentalization by DHX9 stress granules, Cell (2024), https://doi.org/10.1016/j.cell.2024.02.028

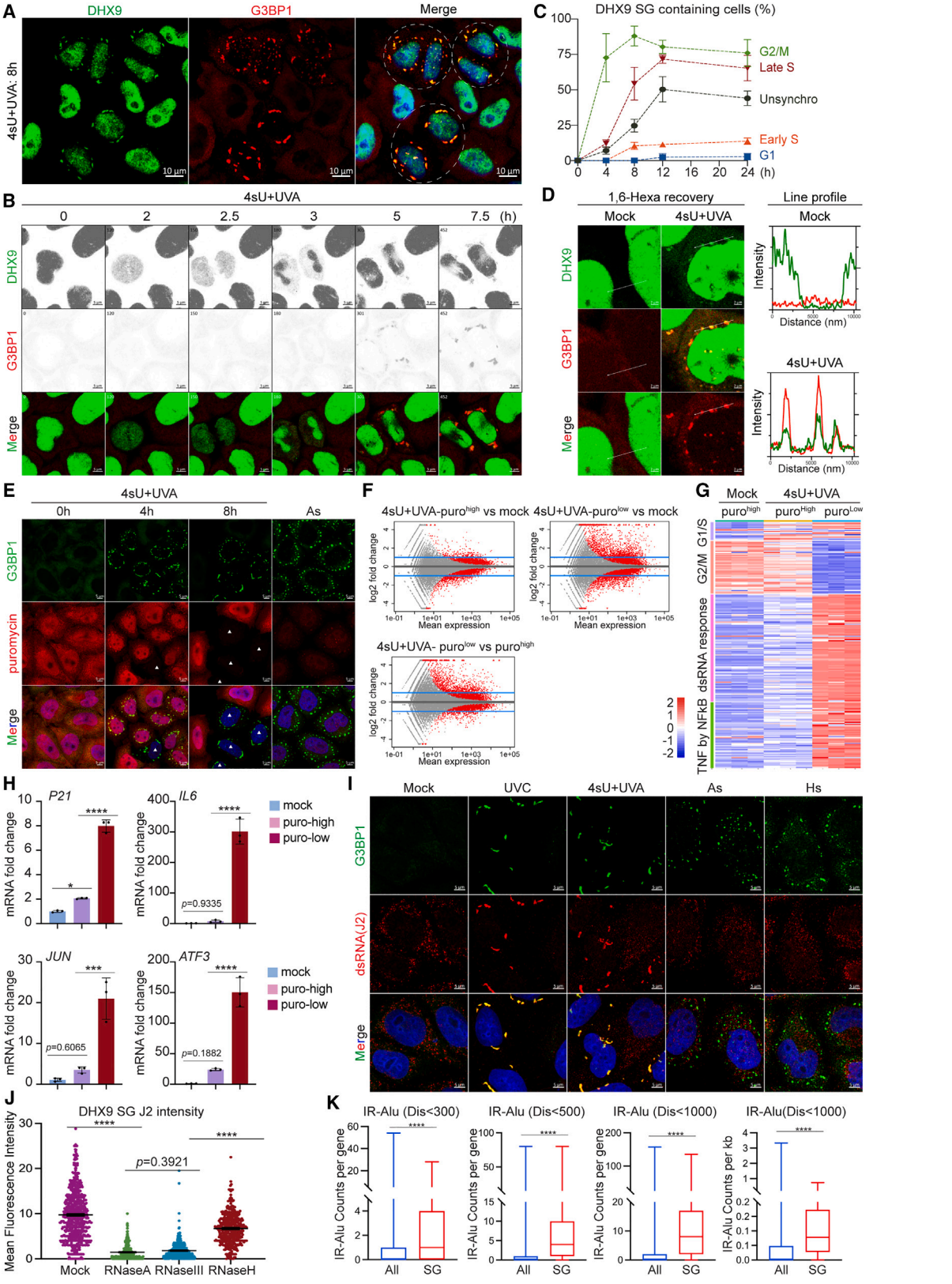

(legend on next page)

Please cite this article in press as: Zhou et al., RNA damage compartmentalization by DHX9 stress granules, Cell (2024), https://doi.org/10.1016/j.cell.2024.02.028

dsRNA in the cell,[35,36] and interestingly, the introns enriched in 4sU + UVA-induced DHX9 SGs contained more IR-*Alu* pairs, compared with introns on average, regardless of intron length (Figure 4K).

DHX9 modulates dsRNA abundance in DHX9 SGs

As a major and specific protein component of 4sU + UVA- and UVC-induced SGs, we wanted to determine the role of DHX9 within the SGs. We established a cell line in which the endogenous *DHX9* locus was tagged using an auxin-inducible degron sequence to permit rapid degradation of DHX9 protein (Figure 5A). Although depletion of DHX9 did not abrogate assembly of 4sU + UVA-induced SGs, the SGs elicited in DHX9-depleted cells contained more dsRNA than controls (Figure 5B and 5C). Knockdown of DHX9 by siRNA gave a consistent result and showed higher expression of dsRNA-related immune responsive genes, compared with control cells (Figures S7A and S7B). Cell-cycle synchronization experiments (Figure S7C) revealed that DHX9-depleted cells only mounted a substantial transcriptional dsRNA stress response when 4sU + UVA was administered in the previous mother cell generation (Figures 5D–5I). Depletion of DHX9 had no effect if RNA crosslinking damage was administered directly in the same cell generation, corroborating the idea that DHX9 contributes toward the modulation of dsRNA level in the SGs. Much higher rates of cell death were observed in DHX9-depleted daughter cells following parental acquisition of 4sU + UVA-induced RNA crosslinking damage (Figures 5J and 5K). Moreover, splicing inhibitors also caused a higher immune response in DHX9-depleted cells, compared with control cells (Figure S7D). We further observed a dose-dependent suppression of cell proliferation following exposure to 4sU + UVA treatment, which was aggravated in DHX9-depleted cells (Figure 5L). Taken together, the data suggest that DHX9 is critical to enable daughter cells to modulate dsRNA levels in the SGs and protect them from the deleterious dsRNA immune response.

Our previous work showed that DHX9 binds to dsRNA structures contained in mRNA.[35] Interestingly, the intron-containing transcripts enriched in DHX9 SGs have more DHX9-binding sites than the average transcript expressed in the same cells (Figure S7E), suggesting that DHX9 may bind to dsRNA secondary structure-containing introns in DHX9 SGs. *In vitro* phase separation assays showed that DHX9 preferentially forms condensates with dsRNA, such as mammalian IR-*Alu* RNA or *D. melanogaster roX2* RNA, but not with single strand (ss)RNA, including *Alu* and *luciferase* mRNA (Figures S7F–S7H). Interestingly, while deletion of either the dsRNA binding domain (RBD) or arginine–glycine–glycine repeat (RGG) domains abolished localization of DHX9 to the SGs, the helicase-dead mutation (GET) promoted recruitment of DHX9 to the SGs (Figure 5M). Only wild-type (WT) DHX9, but not the ΔRBD, ΔRGG, or helicase-dead mutants, can restore expression of the immune gene *ATF3* in DHX9-depleted cells (Figure 5N). Taken together, our data suggest that DHX9 is critical to enable daughter cells to modulate dsRNA levels in the SGs and protect them from the deleterious dsRNA immune response.

G3BP1/2 drives DHX9 SG assembly

Classical SGs are believed to form through phase separation of G3BP1/2 with free mature mRNA in the cytosol.[17,37] G3BP1 and G3BP2 play redundant roles in the cells, and we established *G3BP1* knockout (KO) cells but failed to generate a constitutive double *G3BP1/G3BP2* KO cell line. To circumvent this, we made a cell line with the *G3BP1* locus knocked out and the endogenous *G3BP2* gene tagged with the auxin-inducible degron tag (Figure S8A).[38] We validated the efficient depletion of both G3BP1 and G3BP2 proteins in this cell line after auxin induction for 30 min. Henceforth we refer to these cells in the auxin-treated condition as G3K cells (Figure S8B). As- and poly(I:C)-induced SG assembly was blocked in G3K cells, as shown by the lack of cytoplasmic granule structures marked with SG marker HuR (Figure S8C). Interestingly, DHX9 SGs

Figure 4. UV induces DHX9 SGs in daughter cells

(A) Representative confocal images of DHX9 and G3BP1 in HeLa cells 8 h after 4sU + UVA stress. Scale bars, 10 μm. White dashed circles mark paired DHX9 SGs-containing cells.

(B) Representative frames from time-lapse live-cell imaging of DHX9-eGFP and G3BP1-mCherry signals in HeLa cells treated with 4sU + UVA. Scale bars, 5 μm.

(C) Quantification of the percentage of cells exhibiting DHX9 SGs at different time points. Cells were synchronized at indicated cell-cycle stages and treated with 4sU + UVA and simultaneously released from the synchronization. Data are shown as mean ± SEM (n = 3 biological replicates from 2 independent experiments).

(D) Representative confocal images (left) and quantification (right) of DHX9-eGFP and G3BP1-mCherry signals along the indicated white lines. Images are zoomed from those shown in Figure S6C.

(E) Representative images of G3BP1 and puromycin staining in HeLa cells treated with the indicated stresses. The cells were labeled with puromycin (10 μg/mL) for 10 min before fixation. Scale bars, 5 μm. White arrows mark puromycin^{low} cells.

(F) M-versus-A (MA) plots of gene expression comparing mock (puromycin^{high}), 4sU + UVA-treated puromycin^{low}, and 4sU + UVA-treated puromycin^{high} cells.

(G) Heatmap showing expression of gene categories including G1/S, G2/M, dsRNA immune response, and TNF signaling by NF-κB. The lists of G1/S and G2/M genes are taken from the published literature.[31] The gene list of "TNF by NF-κB" is from the Human Gene Set (M5890). The gene list of "dsRNA response" is from the Human Gene Set (M8789).

(H) RT-qPCR assays quantifying changes in expression of the indicated genes in puro^{high} and puro^{low} FACS-sorted HeLa cells. The y axis shows relative mRNA level normalized to the mock sample for each gene. Data are shown as mean ± SEM (n = 3 technical replicates from a representative experiment out of 3 independent experiments). Significance was scored by ordinary one-way ANOVA, *p<0.05, ****p<0.0001

(I) Representative confocal images of G3BP1 and dsRNA(J2) signals in HeLa cells treated with the indicated stresses. Scale bars, 5 μm.

(J) Quantification of dsRNA(J2) signal in DHX9 SGs from 4sU + UVA-stressed HeLa cells treated with the indicated enzymes after fixation. Scale bars, 5 μm. Representative data from three biological replicates are shown as mean ± SEM, each dot indicates one SG. Significance was scored by non-parametric one-way ANOVA followed by a Kruskal-Wallis test, ****$p < 10^{-15}$.

(K) IR-*Alu* pairs are defined as pairs of inverted repeat *Alu* elements located within the indicated distance of each other (see STAR Methods). Distances are given in bp. Boxplots show the IR-*Alu* pairs numbers and density on genes expressed in the cells (all) and genes with intron enrichment in DHX9 SGs (SG). Center line: median; box limits: 25th to 75th percentiles; whiskers: min to max. Significance was scored by the Poisson test. ****$p < 10^{-15}$.

See also Figure S6 and Videos S3 and S4.

Please cite this article in press as: Zhou et al., RNA damage compartmentalization by DHX9 stress granules, Cell (2024), https://doi.org/10.1016/j.cell.2024.02.028

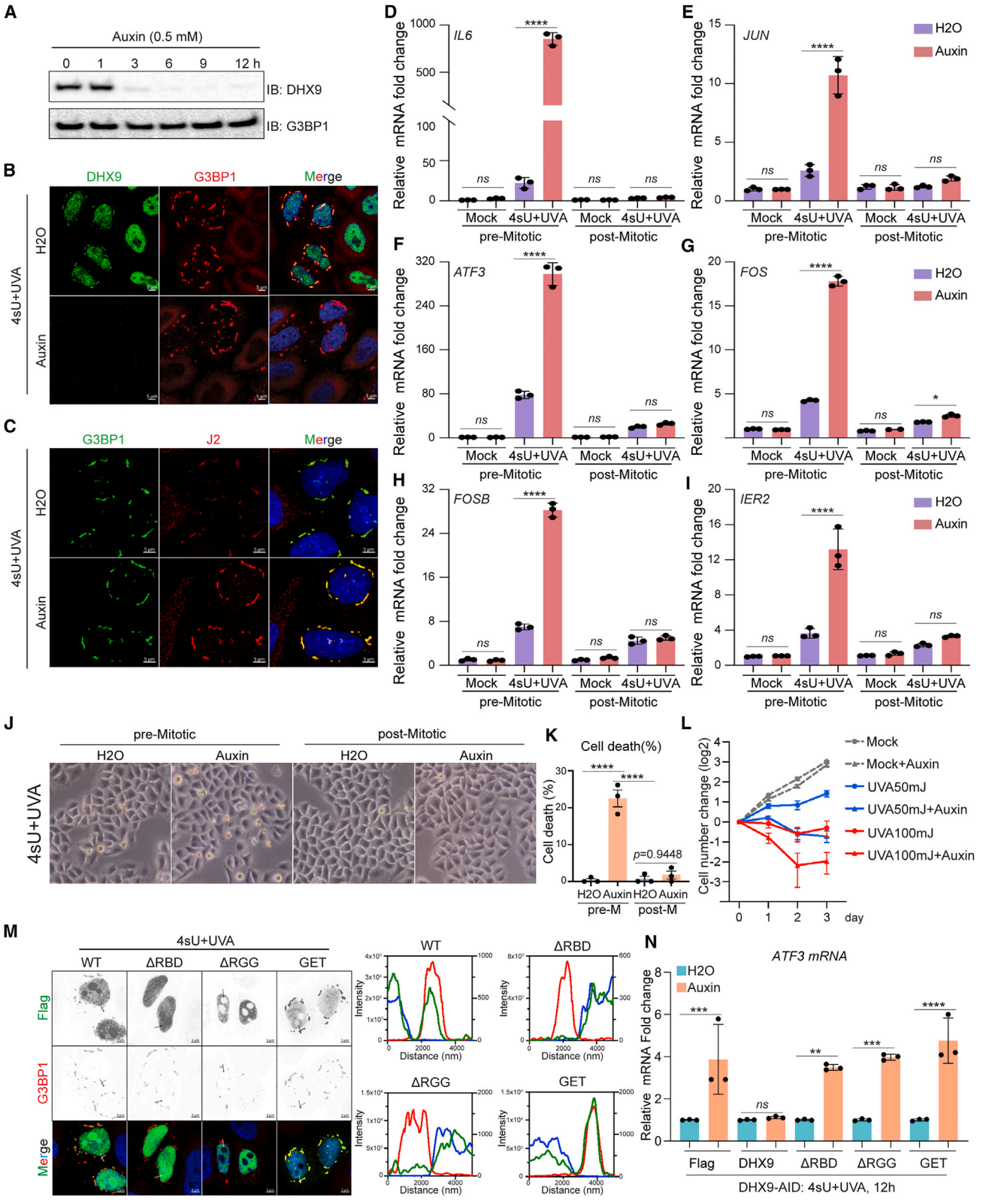

(legend on next page)

Please cite this article in press as: Zhou et al., RNA damage compartmentalization by DHX9 stress granules, Cell (2024), https://doi.org/10.1016/j.cell.2024.02.028

were not formed upon 4sU + UVA stress in G3K cells, but the cytosolic retention of DHX9 and HNRNPM; two DHX9 SG-specific markers; as well as HuR, a universal SG marker, were preserved in these cells, and a part of the DHX9/HNRNPM even formed tiny foci in the cytoplasm (Figure 6A). We further confirmed this phenomenon by knocking down G3BP2 by siRNA in G3BP1 KO cells (Figure S8D).

The current model of SG formation suggests that classical SGs are downstream of and dispensable for translation shutdown induced by stress kinase (HRI, PKR, PERK, and GCN2)-mediated eIF2a phosphorylation.[14,39] In line with this model, As- or poly(I:C)-induced translation arrest still took place in G3K cells (Figure S8E). On the other hand, 4sU + UVA-stress-induced translation shutdown was abolished in G3K cells (Figures 6B and 6C). eIF2a phosphorylation is the upstream signal of translation shutdown. 4sU + UVA stress induced eIF2a phosphorylation mainly in DHX9 SG-containing cells (Figure S8F). Interestingly, while 4sU + UVA treatment activated eIF2a phosphorylation in DHX9 SG-containing WT cells, G3K cells showed no eIF2a phosphorylation, irrespective of whether the cells exhibited cytoplasmic retention of HNRNPM or not (Figure 6E). Consistently, while the assembly of SGs induced by As, poly(I:C), and 4sU + UVA were all inhibited in G3K cells (as shown by the lack of intact granule structures marked with the SG marker HuR), eIF2a phosphorylation was only impaired in 4sU + UVA-treated G3K cells (Figures 6D and S8G). These data suggested that assembly of DHX9 SGs was essential for triggering the translation shutdown upon 4sU + UVA treatment, while As- and poly(I:C)-induced SGs were dispensable for translation arrest. Moreover, while dsRNA was significantly enriched in DHX9 SGs in WT cells, there were no detectable dsRNA foci observed in G3K cells after 4sU + UVA stress (Figure S8H). A previous study showed that complementation of G3BP1/2 double-knockout (DKO) cells with WT G3BP1 or a synthetic G3BP1 mimic, but not a G3BP1 ΔNTF2 domain mutant, was able to mediate SG formation after As treatment.[17] We observed that 4sU + UVA-treated G3K cells complemented with WT or synthetic G3BP1 assemble DHX9 SGs and exhibit translation shutdown. However, G3K cells expressing ΔNTF2 G3BP1 do not form SGs and maintain translation activity after 4sU + UVA treatment (Figure S8I), indicating that the assembly of DHX9 SGs, but not other functions of G3BP1/2, is the main contributor to translation shutdown caused by 4sU + UVA stress. Interestingly, G3K cells exhibited lower immune response after 4sU + UVA treatment and were more sensitive to both UVB and 4sU + UVA stresses (Figures 6F, 6G, and S8J). These data suggest that the DHX9 SGs in daughter cells have a cytoprotective role against parental RNA damage, and assembly of DHX9 SGs is crucial for turning off translation and activating immune responses in daughter cells.

PKR and HRI are the eIF2a kinases that are activated by dsRNA and As, respectively. Knockdown of HRI and PKR by siRNAs prevented classical SG formation by As and poly(I:C), respectively, but did not influence DHX9 SG formation upon 4sU + UVA stress (Figure S9A). Moreover, knockdown of HRI and PKR did not trigger eIF2a phosphorylation in unstressed cells, but HRI knockdown prevented As-induced eIF2a phosphorylation (Figures S9B and S9C). On the other hand, PKR knockdown prevented both 4sU + UVA- and poly(I:C)-induced eIF2a phosphorylation (Figures 6H and S9D). Puromycin labeling experiments showed consistent results in which HRI knockdown prevented As-induced translation arrest, whereas PKR knockdown prevented poly(I:C)- and 4sU + UVA-induced translation arrest (Figures 6I, 6J, and S9E–S9H). These results indicate that DHX9 SGs induce translation shutdown through the PKR-eIF2a signaling axis. Overall, our data reveal that DHX9 SGs and classical SGs show distinct molecular mechanisms whereby DHX9 SGs induce translation shutdown but classical SGs are induced by translation shutdown (Figure S9I).

Autophagy receptor p62 promotes DHX9 SG disassembly

Our FANCI-mass spectrometry data further revealed that the 4sU + UVA-induced SG proteome is distinct from the As- and Hs-induced classical SG proteomes (Figure S9J). In line with the increased abundance of long intron-containing transcripts scored in the FANCI RNA-seq data, there were over 50 pre-mRNA-binding proteins enriched in DHX9 SGs but not in As- and Hs-induced classical SGs (Figures 7A and S10A; Table S2). GO and STRING protein interaction analysis showed a strong enrichment of nuclear localized mRNA processing and splicing process annotations for proteins enriched in DHX9

Figure 5. DHX9 modulates dsRNA abundance in DHX9 SGs

(A) Immunoblot of *DHX9-AID; Myc-Tir1* HeLa cells treated with auxin. G3BP1 is used as the loading control.

(B and C) Representative confocal images of DHX9 (B) or G3BP1 (C) and J2 signals in *DHX9-AID; Myc-Tir1* HeLa cells treated as indicated. Auxin is added immediately after UVA. Scale bars, 5 μm.

(D–I) RT-qPCR assays quantifying the gene expression changes in *DHX9-AID; Myc-Tir1* HeLa cells subjected to 4sU + UVA stress either in the parental cell generation (pre-mitotic) or in the daughter cells (post-mitotic). The experimental design is shown in Figure S7C. The y axis shows mRNA levels normalized to the mock H_2O sample for each condition. Data are shown as mean ± SEM (n = 3 technical replicates from a representative experiment out of 3 independent experiments). Significance was scored by one-way ANOVA, ns: p>0.05, *p<0.05, ****p<0.0001

(J and K) Representative images (J) and quantification (K) of cell death of cells treated as shown in Figure S7C. The images were taken 24 h after 4sU + UVA treatment. Data are shown as mean ± SEM (n = 3 biological replicates from 2 independent experiments). Significance was scored by one-way ANOVA, ****p<0.0001

(L) *DHX9-AID; Myc-Tir1* HeLa cell growth curve after 4sU + UVA and auxin treatment, as indicated. Auxin is added immediately after 4sU + UVA stress but removed after 24 h. The y axis depicts the $\log_2$ fold change, and data are shown as mean ± SEM (n = 3 biological replicates from 2 independent experiments).

(M) Representative confocal images and quantification of FLAG-DHX9 (green), G3BP1 (red), and DAPI (blue) signals across the drawn white lines in HeLa cells transiently overexpressing the indicated FLAG-tagged DHX9 mutants and treated with 4sU + UVA.

(N) RT-qPCR assays quantifying the *ATF3* mRNA expression changes in *DHX9-AID; Myc-Tir1* HeLa cells expressing the indicated DHX9 mutants for 18 h and subjected to 4sU + UVA stress with H_2O or auxin treatments for 8 h. Significance was scored by one-way ANOVA, ns: p>0.05, **p<0.01, ***p<0.001, ****p<0.0001. See also Figure S7.

Please cite this article in press as: Zhou et al., RNA damage compartmentalization by DHX9 stress granules, Cell (2024), https://doi.org/10.1016/j.cell.2024.02.028

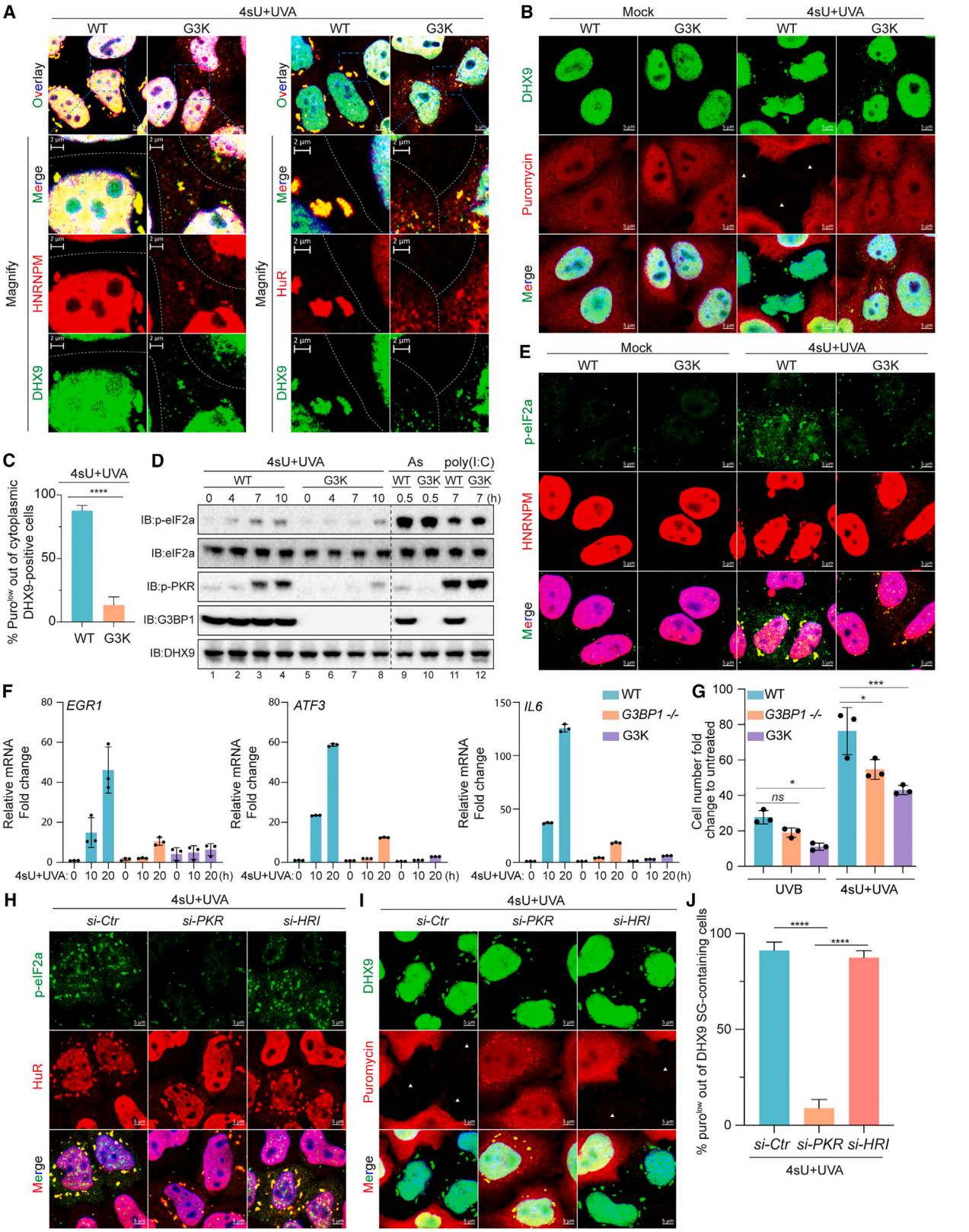

(legend on next page)

Please cite this article in press as: Zhou et al., RNA damage compartmentalization by DHX9 stress granules, Cell (2024), https://doi.org/10.1016/j.cell.2024.02.028

SGs, while translation-related processes are enriched in proteins found in As- and Hs-induced SGs (Figures 7B and S10B). The localization of several proteins showing the highest enrichment in DHX9 SGs in our mass spectrometry data (HNRNPA0, HNRNPA1, HNRNPA3, HNRNPM, and TDP43) was validated in both 4sU + UVA- and UVC-induced DHX9 SGs, using immunofluorescence (Figures S10C–S10G). Furthermore, we identified MATR3 as a protein localizing to 4sU + UVA-induced but not to UVC-induced DHX9 SGs, which indicates that subtle differences may exist within different DHX9 SG subtypes (Figure S10H). Moreover, we analyzed the publicly available ENCODE eCLIP datasets for five RNA-binding proteins (RBPs) highly enriched in DHX9 SGs (HNRNPA1, NONO, TDP43, FUS, and HNRNPM).[40] Our analysis revealed a higher-than-expected enrichment of intron-containing RNAs, which can be bound by these RBPs within DHX9 SGs (as identified through FANCI RNA-seq), in comparison with the proportion of these intron-containing RNAs in the entire cell (Figure S10I). These data suggest that specific RNA-protein interactions may contribute to their sequestration into DHX9 SGs.

An interesting question given the importance of stress resolution is how these granules are disassembled.[41] We found that the autophagy receptor p62, but not VCP, is highly enriched in DHX9 SGs but not As-induced SGs (Figure 7C). Interestingly, p62 immunofluorescence staining showed that p62 but not VCP autophagosomes are specifically formed in DHX9 SG-containing cells and appear co-localized with or proximal to DHX9 SGs (Figures 7D and S10J). Interestingly, knockdown of p62 by siRNA did not disturb DHX9 SG formation but prevented DHX9 SG disassembly (Figure 7E). In line with this, knockdown of p62 sensitized cells to UV stress and led to a higher immune response, compared with control cells (Figures 6F and 6G).

DISCUSSION

During the cell cycle, daughter cells not only acquire genomic information but also inherit non-genetic contents from mother cells. Studies in yeast, *D. melanogaster*, and mammalian species indicated that mRNA inheritance has a profound impact on the fate of daughter cells.[9,42–44] Here, we show that daughter cells assemble non-membranous cytoplasmic DHX9 SGs to sequester RNA-protein crosslinking damaged parental intron RNA and recruit DHX9 to modulate the dsRNA stress, highlighting the fact that daughter cells not only passively inherit parental material but can also discern and segregate the damaged one.

Previous studies failed to establish a molecular link between UVC-induced DNA damage and UVC-induced SGs. Notably, a study conducted by Jan H.J. Hoeijmakers' group 14 years ago demonstrated that cells lacking XPA, Ku70, Ku80, DNA-PK, RAD54, Nbs1, p53, or Dicer still exhibited the formation of these distinctive SGs following UVC stress.[45] We have now not only validated several of these key observations but also for the first time demonstrated that RNA crosslinking damage, but not DNA damage, is the major trigger of UVC-induced SGs, and these SGs are important for cell survival, dsRNA-related immune response, and translation shutdown in daughter cells, differentiating them from classical SGs that assemble downstream of and are dispensable for translation arrest.

An interesting question in cell biology is how the stress response is ultimately terminated by cells. Autophagy is a conserved system that removes unnecessary or damaged components through lysosomal degradation.[46] Selective autophagy is mediated by autophagy receptors that bridge the cargo and phagophore. Various selective autophagy receptors have been shown to recognize different organelles in the cell.[46] Here, we found that p62 but not VCP autophagy is activated to disassemble DHX9 SGs and promotes cell survival after RNA damage stress. p62 is reported to directly bind small non-coding RNA vtRNAs.[47] It would be interesting to further explore whether and what damaged intron RNA is recognized by p62.

Several other degradation mechanisms have been uncovered to process abnormal mature mRNA. Ribosome stalling by strong RNA secondary structure can activate the No-Go decay pathway through ribosome collision.[48,49] Mature mRNA oxidation and alkylation damage have been shown to cause translation blockage and thus also activate the No-Go decay pathway.[50] However, the cellular response to damaged

Figure 6. G3BP1/2 drives DHX9 SG assembly

(A) Representative confocal images of DHX9 and HNRNPM or HuR in WT and G3K HeLa cells 8 h after 4sU + UVA stress. Auxin was added immediately after 4sU + UVA stress. HuR is a universal marker for all SG subtypes, while HNRNPM is a DHX9 SG-specific marker identified by FANCI-DHX9-SG proteomics. Scale bars, top, 5 μm and bottom, 2 μm. G3K: auxin-treated *G3BP1*$^{-/-}$*; G3BP2-AID; Myc-Tir1* HeLa, see Figure S8B. Images were saturated to display the cytosolic retention of indicated proteins.

(B and C) Representative images (B) and quantification (C) of DHX9 and puromycin staining in HeLa cells treated with the indicated stresses. Puromycin was added to the culture medium 10 min before collection. Scale bars, 5 μm. White arrows mark puromycin^{low} cells. Images were saturated to display the cytosolic retention of DHX9. Significance was scored by unpaired t test with Welch's correction, ****p<0.0001.

(D) Immunoblot of eIF2a and PKR phosphorylation in WT and G3K HeLa cells treated with indicated stresses. DHX9 is used as the loading control.

(E) Representative images of HNRNPM and p-eIF2a staining in HeLa cells treated with 4sU + UVA. Scale bars, 5 μm. Images were saturated to display the cytosolic retention of HNRNPM.

(F) RT-qPCR assays quantifying changes of indicated genes in indicated HeLa cells with 4sU + UVA stress. Data are shown as mean ± SEM. Values are normalized to the mock sample of WT HeLa cell lines (n = 3 technical replicates from a representative experiment out of 3 independent experiments).

(G) G3BP1 KO and G3K HeLa cells were treated with either UVB (50 mJ/cm^2) or 4sU + UVA (100 mJ/cm^2) stress, and after 48 h, the cell number was counted and plotted normalized to unstressed cells of the corresponding genotype. Significance was scored by ordinary one-way ANOVA, ns: p>0.05, *p<0.05, ***p<0.001.

(H and I) Representative images of indicated proteins or puromycin staining in HeLa cells fixed 44 h after transfection with the indicated siRNAs and 8 h after treatment with 4sU + UVA. Puromycin was added to culturing medium 10 min before collection. White arrows mark puromycin^{low} cells. Scale bars, 5 μm.

(J) Quantification of puromycin^{low} HeLa cells among all DHX9 SG-positive HeLa cells shown in (I). Mean ± SEM (n = 3 biological replicates from 2 independent experiments). Significance was scored by ordinary one-way ANOVA, ****p<0.0001.

See also Figures S8 and S9.

Please cite this article in press as: Zhou et al., RNA damage compartmentalization by DHX9 stress granules, Cell (2024), https://doi.org/10.1016/j.cell.2024.02.028

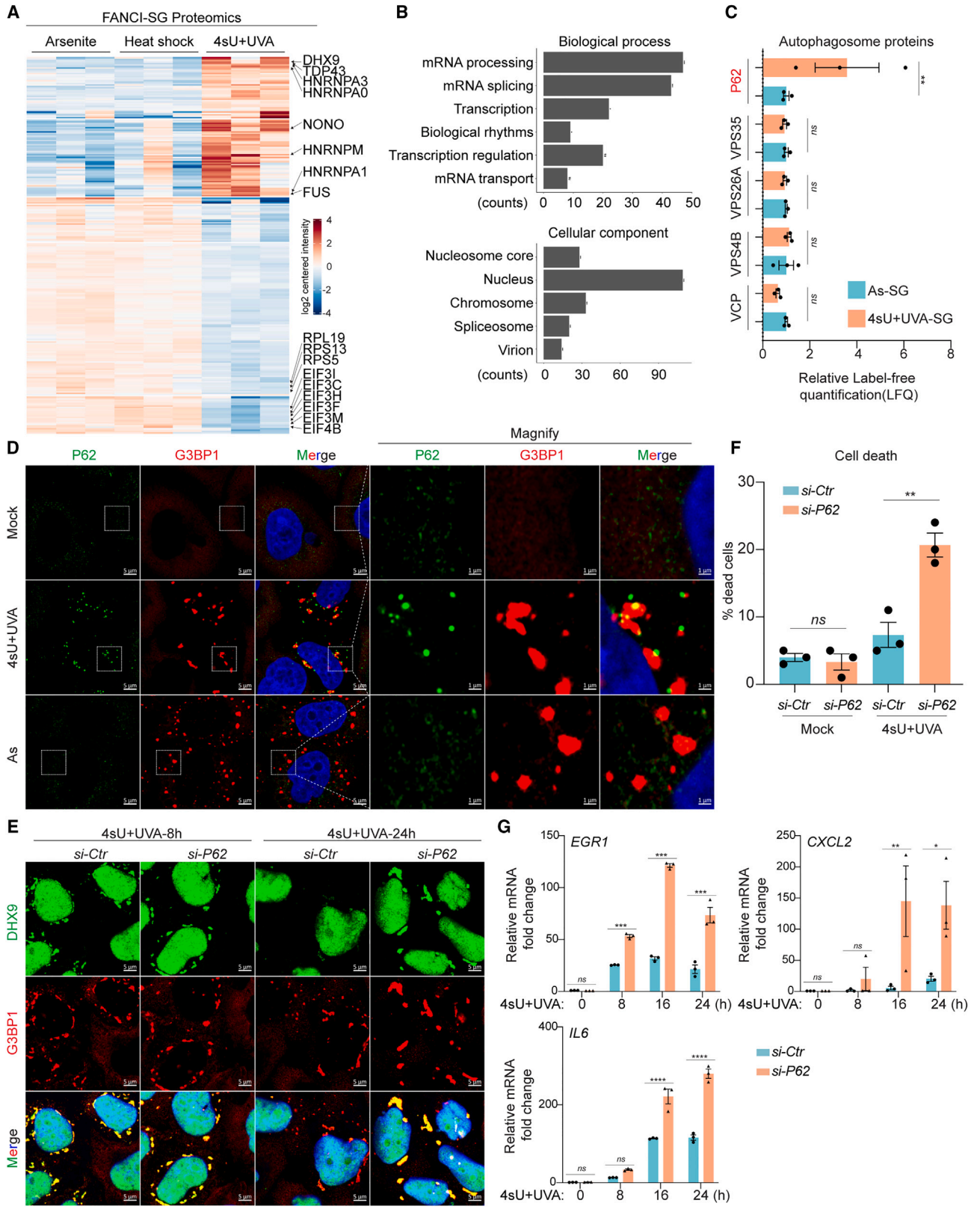

(legend on next page)

Please cite this article in press as: Zhou et al., RNA damage compartmentalization by DHX9 stress granules, Cell (2024), https://doi.org/10.1016/j.cell.2024.02.028

intron-containing RNAs had not been characterized to date. A recent study showed that UVB/C-induced RNA crosslinking damage elicits pyroptosis through a recently characterized dsRNA sensor NLRP1.[51] An interesting question to be investigated by future studies is whether UV-induced pyroptosis might in fact be mediated by intronic RNA rather than mature mRNA damage and be daughter cell specific as well.

The cytoplasm is the primary intracellular compartment to be breached by virus infections, and to mediate a timely response, this compartment is host to multiple viral dsRNA sensors, including MDA5, DDX58, and PKR.[52] On the other hand, two abundant dsRNA helicases, DHX9 and SUV3, localize exclusively to the nucleus and mitochondria to eliminate nuclear and mitochondrial endogenous dsRNA, respectively.[35,53] Compartmentalizing mitochondrial and nuclear dsRNA-containing transcripts into discrete compartments and equipping them with dedicated dsRNA RNA helicases represents an elegant strategy by the cell to locally deal with endogenous dsRNA while still permitting the cytosol to efficiently respond to invading viral dsRNA. Here, we found that under UV and splicing defect stress conditions, DHX9 engages an "emergency" cellular mechanism by migrating to cytoplasmic SGs to alleviate cytosolic self-dsRNA stress. Some viruses seem to be capable of hijacking this emergency mechanism by recruiting DHX9 to cytoplasmic viral replication factories, enabling the remodeled viral RNA to pass off as "self" and avoid triggering the dsRNA immune response.[54–57] It would be interesting to further investigate the molecular mechanism by which DHX9 is recruited to cytoplasmic SGs and viral replication factories and the possible relationship to the cell cycle in the future.

Limitations of the study

Although we quantified RNA-protein crosslinking by analyzing RNA T>C mismatches, we did not measure the possible RNA-RNA crosslinking damage that may also be caused by UV. Additional measurements like reverse transcriptase pausing assay or long-read RNA-seq might be helpful to address this question. While our study extensively explored the role of DHX9 in UV-induced SGs, DHX9 is unlikely to be the sole helicase responsive to and regulating this complex cellular stress response. The SG-specific roles of many other proteins identified in the DHX9 SG proteome, including DDX5, DDX17, and DDX20, remain uncharacterized. It is unclear from this study whether these helicases play roles in the stress response and what RNA they target. Moreover, although we observed the presence of DHX9 SGs in HeLa cells and three different keratinocyte cell lines, as well as in a HEE model upon UV treatments, we did not explore DHX9 SGs and related dsRNA immune responses in human or mouse skin tissues.

STAR★METHODS

Detailed methods are provided in the online version of this paper and include the following:

- KEY RESOURCES TABLE
- RESOURCE AVAILABILITY
  - Lead contact
  - Materials availability
  - Data and code availability
- EXPERIMENTAL MODEL AND STUDY PARTICIPANT DETAILS
  - Cell culture
  - Generation of endogenous tagged cell lines
- METHOD DETAILS
  - Stress treatments
  - FANCI
  - LC-MS analysis
  - MS data analysis
  - Puro-seq
  - Cell synchronization
  - Transient transfection
  - RNA decay
  - Live cell imaging
  - Immunofluorescence
  - Correlative light and electron microscopy (CLEM)
  - Electron microscopy
  - Protein purification
  - Cy3-labelled RNA synthesis
  - In vitro phase separation
  - Protein extraction and Western blot
  - Quantitative reverse transcription PCR (RT-qPCR)
  - DNA Dot Blot
  - Human epidermal equivalent (HEE) generation
  - Crystal Violet Stain
  - Comet assay

Figure 7. Autophagy receptor p62 promotes DHX9 SG disassembly

(A) Heatmap of proteins differentially enriched in DHX9 SGs and canonical (As- and Hs-induced) SGs from mass spectrometry experiments. Each sample includes three biological replicates.

(B) DAVID biological process and cellular component analysis of proteins enriched in DHX9 SGs. Only top categories as reported by DAVID are shown.

(C) Relative label-free quantification (LFQ) of all autophagy-related proteins detected in FANCI-SG proteomics data, also seen in Table S2. Student's t test, ns: $p>0.05$, $^{**}p<0.01$.

(D) Representative images of G3BP1 and p62 staining in HeLa cells treated with the indicated stresses. Scale bars, left, 5 μm and right, 1 μm. White dashed line marks the magnified region.

(E) Representative images of G3BP1 and DHX9 staining in p62-depleted HeLa cells 8 and 24 h after 4sU + UVA treatment. Scale bars, 5 μm.

(F) Percentage of cell death in control and p62-depleted HeLa cells stressed with 4sU + UVA (100 mJ/cm^2). (n = 3 biological replicates from 2 independent experiments.) Significance was scored by one-way ANOVA, ns: $p>0.05$, $^{**}p<0.01$.

(G) RT-qPCR assays quantifying changes of indicated dsRNA immune responsive genes in control and p62 siRNA-treated HeLa cells stressed with 4sU + UVA. Data are shown as mean ± SEM (n = 3 biological replicates from 2 independent experiments). Values are normalized to the si-Ctr 0-h sample. Significance was scored by two-way ANOVA followed by a Bonferroni test, ns: $p>0.05$, $^{*}p<0.05$, $^{**}p<0.01$, $^{***}p<0.001$, $^{****}p<0.0001$.

See also Figure S10 and Table S2.

SUPPLEMENTAL INFORMATION

Supplemental information can be found online at https://doi.org/10.1016/j.cell.2024.02.024.

ACKNOWLEDGMENTS

We thank the past and current members of the Akhtar lab for helpful discussions and support, especially Tuğçe Aktaş and Ibrahim Ilik for plasmids, Yidan Sun for FLASH data analysis, Sheng Hu Qian for IR-*Alu* identification, and Tanvi Kulkarni for *roX2* and *luciferase* RNA generation. We thank Eray Mehmet Akbas for creating the graphical abstract. We thank the scientific core facilities in MPI Freiburg for help in experiments. We are grateful to Dr. Oliver T. Fackler and Dr. Ellen van den Bogaard for providing pWPI-Neo IRF3.GFP vector and N/TERT-1 cells, respectively. We thank Prof. J. Paul Taylor kindly for G3BP1 constructs. We thank Prof. Ute Woelfle for sharing the HaCAT cell line. We thank Dr. Eirini Trompouki and Dr. Nicola Iovino for critical reading of the manuscript. This study was supported by the German Research Foundation (DFG) under Germany's Excellence Strategy (CIBSS—EXC-2189—project ID 390939984). This work was also supported by the German Research Foundation (DFG) under the CRC 992 (A02), CRC 1425 (P04), and CRC 1381 (B3) awarded to A.A. Y. Zhou was supported by the European Molecular Biology Organization (EMBO) Postdoctoral Fellowship. This work was also supported by the award of the Gottfried Wilhelm Leibniz Prize by the German Research Foundation (DFG) to A.A.

AUTHOR CONTRIBUTIONS

Y. Zhou conceptualized the study with A.P., M.S., and A.A. Y. Zhou performed the experiments, data analyses, and wrote the manuscript with the help of A.P., M.S., H.H., N.U.E., I.G., J.S., A.G.-A., and G.M. H.H. performed protein expression and purification. A.G.-A. and G.M. performed MS experiments. M.H. and S.K. performed correlative light and electron microscopy (CLEM) experiments at the Core Facility for Electron Microscopy (EMcore [RI_00555]) at the University Freiburg Medical Center. M.B. and Y. Zhao analyzed RNA-seq data with guidance from T.M. A.A. acquired funding and supervised all aspects of the study.

DECLARATION OF INTERESTS

The authors declare no competing interests.

Received: July 5, 2023
Revised: October 24, 2023
Accepted: February 22, 2024
Published: March 18, 2024

REFERENCES

1. Rastogi, R.P., Richa Kumar, A., Tyagi, M.B., and Sinha, R.P. (2010). Molecular mechanisms of ultraviolet radiation-induced DNA damage and repair. J. Nucleic Acids *2010*, 592980.
2. Pfeifer, G.P. (1997). Formation and processing of UV photoproducts: effects of DNA sequence and chromatin environment. Photochem. Photobiol. *65*, 270–283.
3. Yoon, J.H., Lee, C.S., O'Connor, T.R., Yasui, A., and Pfeifer, G.P. (2000). The DNA damage spectrum produced by simulated sunlight. J. Mol. Biol. *299*, 681–693.
4. Syed, D.N., Afaq, F., and Mukhtar, H. (2012). Differential activation of signaling pathways by UVA and UVB radiation in normal human epidermal keratinocytes. Photochem. Photobiol. *88*, 1184–1190.
5. Sample, A., and He, Y.-Y. (2018). Mechanisms and prevention of UV-induced melanoma. Photodermatol. Photoimmunol. Photomed. *34*, 13–24.
6. De Fabo, E.C., Noonan, F.P., Fears, T., and Merlino, G. (2004). Ultraviolet B but not ultraviolet A radiation initiates melanoma. Cancer Res. *64*, 6372–6376.
7. Blondel, M.O., and Favre, A. (1988). tRNAPhe and tRNAPro are the near-ultraviolet molecular targets triggering the growth delay effect. Biochem. Biophys. Res. Commun. *150*, 979–986.
8. Ramabhadran, T.V., Fossum, T., and Jagger, J. (1976). In vivo induction of 4-thiouridine-cytidine adducts in tRNA of E. coli B/r by near-ultraviolet radiation. Photochem. Photobiol. *23*, 315–321.
9. Shlyakhtina, Y., Moran, K.L., and Portal, M.M. (2019). Asymmetric inheritance of cell fate determinants: focus on RNA. Noncoding. RNA *5*, 38.
10. Ule, J., Hwang, H.-W., and Darnell, R.B. (2018). The future of cross-linking and immunoprecipitation (CLIP). Cold Spring Harb. Perspect. Biol. *10*, a032243.
11. Vieira-Vieira, C.H., and Selbach, M. (2021). Opportunities and challenges in global quantification of RNA-protein interaction via UV cross-linking. Front. Mol. Biosci. *8*, 669939.
12. Herzog, V.A., Reichholf, B., Neumann, T., Rescheneder, P., Bhat, P., Burkard, T.R., Wlotzka, W., von Haeseler, A., Zuber, J., and Ameres, S.L. (2017). Thiol-linked alkylation of RNA to assess expression dynamics. Nat. Methods *14*, 1198–1204.
13. Aulas, A., Fay, M.M., Lyons, S.M., Achorn, C.A., Kedersha, N., Anderson, P., and Ivanov, P. (2017). Stress-specific differences in assembly and composition of stress granules and related foci. J. Cell Sci. *130*, 927–937.
14. Protter, D.S.W., and Parker, R. (2016). Principles and properties of stress granules. Trends Cell Biol. *26*, 668–679.
15. Panas, M.D., Ivanov, P., and Anderson, P. (2016). Mechanistic insights into mammalian stress granule dynamics. J. Cell Biol. *215*, 313–323.
16. Lee, C.-Y., and Seydoux, G. (2019). Dynamics of mRNA entry into stress granules. Nat. Cell Biol. *21*, 116–117.
17. Yang, P., Mathieu, C., Kolaitis, R.-M., Zhang, P., Messing, J., Yurtsever, U., Yang, Z., Wu, J., Li, Y., Pan, Q., et al. (2020). G3BP1 is a tunable switch that triggers phase separation to assemble stress granules. Cell *181*, 325–345.e28.
18. Markmiller, S., Soltanieh, S., Server, K.L., Mak, R., Jin, W., Fang, M.Y., Luo, E.C., Krach, F., Yang, D., Sen, A., et al. (2018). Context-dependent and disease-specific diversity in protein interactions within stress granules. Cell *172*, 590–604.e13.
19. Matheny, T., Van Treeck, B., Huynh, T.N., and Parker, R. (2021). RNA partitioning into stress granules is based on the summation of multiple interactions. RNA *27*, 174–189.
20. Hafner, M., Landthaler, M., Burger, L., Khorshid, M., Hausser, J., Berninger, P., Rothballer, A., Ascano, M., Jr., Jungkamp, A.-C., Munschauer, M., et al. (2010). Transcriptome-wide identification of RNA-binding protein and microRNA target sites by PAR-CLIP. Cell *141*, 129–141.
21. Cabral, A.J., Costello, D.C., and Farny, N.G. (2022). The enigma of ultraviolet radiation stress granules: research challenges and new perspectives. Front. Mol. Biosci. *9*, 1066650.
22. Khong, A., Matheny, T., Jain, S., Mitchell, S.F., Wheeler, J.R., and Parker, R. (2017). The stress granule transcriptome reveals principles of mRNA accumulation in stress granules. Mol. Cell *68*, 808–820.e5.
23. Lee, J.E., Cathey, P.I., Wu, H., Parker, R., and Voeltz, G.K. (2020). Endoplasmic reticulum contact sites regulate the dynamics of membraneless organelles. Science *367*, eaay7108.

24. Hubstenberger, A., Courel, M., Bénard, M., Souquere, S., Ernoult-Lange, M., Chouaib, R., Yi, Z., Morlot, J.-B., Munier, A., Fradet, M., et al. (2017). P-body purification reveals the condensation of repressed mRNA regulons. Mol. Cell *68*, 144–157.e5.

25. Rajotte, D., Stearns, C.D., and Kabcenell, A.K. (2003). Isolation of mast cell secretory lysosomes using flow cytometry. Cytometry A *55*, 94–101.

26. Van Damme, R., Li, K., Zhang, M., Bai, J., Lee, W.H., Yesselman, J.D., Lu, Z., and Velema, W.A. (2022). Chemical reversible crosslinking enables measurement of RNA 3D distances and alternative conformations in cells. Nat. Commun. *13*, 911.

27. Chao, S.H., and Price, D.H. (2001). Flavopiridol inactivates P-TEFb and blocks most RNA polymerase II transcription in vivo. J. Biol. Chem. *276*, 31793–31799.

28. Vilborg, A., Passarelli, M.C., Yario, T.A., Tycowski, K.T., and Steitz, J.A. (2015). Widespread inducible transcription downstream of human genes. Mol. Cell *59*, 449–461.

29. Vilborg, A., Sabath, N., Wiesel, Y., Nathans, J., Levy-Adam, F., Yario, T.A., Steitz, J.A., and Shalgi, R. (2017). Comparative analysis reveals genomic features of stress-induced transcriptional readthrough. Proc. Natl. Acad. Sci. USA *114*, E8362–E8371.

30. Rosa-Mercado, N.A., Zimmer, J.T., Apostolidi, M., Rinehart, J., Simon, M.D., and Steitz, J.A. (2021). Hyperosmotic stress alters the RNA polymerase II interactome and induces readthrough transcription despite widespread transcriptional repression. Mol. Cell *81*, 502–513.e4.

31. Dominguez, D., Tsai, Y.-H., Gomez, N., Jha, D.K., Davis, I., and Wang, Z. (2016). A high-resolution transcriptome map of cell cycle reveals novel connections between periodic genes and cancer. Cell Res. *26*, 946–962.

32. Patel, S.S., Belmont, B.J., Sante, J.M., and Rexach, M.F. (2007). Natively unfolded nucleoporins gate protein diffusion across the nuclear pore complex. Cell *129*, 83–96.

33. Ribbeck, K., and Görlich, D. (2002). The permeability barrier of nuclear pore complexes appears to operate via hydrophobic exclusion. EMBO J. *21*, 2664–2671.

34. Schmidt, E.K., Clavarino, G., Ceppi, M., and Pierre, P. (2009). SUnSET, a nonradioactive method to monitor protein synthesis. Nat. Methods *6*, 275–277.

35. Aktaş, T., Avşar Ilık, İ., Maticzka, D., Bhardwaj, V., Pessoa Rodrigues, C., Mittler, G., Manke, T., Backofen, R., and Akhtar, A. (2017). DHX9 suppresses RNA processing defects originating from the Alu invasion of the human genome. Nature *544*, 115–119.

36. Ahmad, S., Mu, X., Yang, F., Greenwald, E., Park, J.W., Jacob, E., Zhang, C.Z., and Hur, S. (2018). Breaching self-tolerance to Alu duplex RNA underlies MDA5-mediated inflammation. Cell *172*, 797–810.e13.

37. Guillén-Boixet, J., Kopach, A., Holehouse, A.S., Wittmann, S., Jahnel, M., Schlüßler, R., Kim, K., Trussina, I.R.E.A., Wang, J., Mateju, D., et al. (2020). RNA-induced conformational switching and clustering of G3BP drive stress granule assembly by condensation. Cell *181*, 346–361.e17.

38. Nishimura, K., Fukagawa, T., Takisawa, H., Kakimoto, T., and Kanemaki, M. (2009). An auxin-based degron system for the rapid depletion of proteins in nonplant cells. Nat. Methods *6*, 917–922.

39. McCormick, C., and Khaperskyy, D.A. (2017). Translation inhibition and stress granules in the antiviral immune response. Nat. Rev. Immunol. *17*, 647–660.

40. ENCODE Project Consortium (2012). An integrated encyclopedia of DNA elements in the human genome. Nature *489*, 57–74.

41. Buchan, J.R., Kolaitis, R.-M., Taylor, J.P., and Parker, R. (2013). Eukaryotic stress granules are cleared by autophagy and Cdc48/VCP function. Cell *153*, 1461–1474.

42. Edelmann, F.T., Schlundt, A., Heym, R.G., Jenner, A., Niedner-Boblenz, A., Syed, M.I., Paillart, J.-C., Stehle, R., Janowski, R., Sattler, M., et al. (2017). Molecular architecture and dynamics of ASH1 mRNA recognition by its mRNA-transport complex. Nat. Struct. Mol. Biol. *24*, 152–161.

43. Wang, J., Wang, L., Feng, G., Wang, Y., Li, Y., Li, X., Liu, C., Jiao, G., Huang, C., Shi, J., et al. (2018). Asymmetric expression of LincGET biases cell fate in two-cell mouse embryos. Cell *175*, 1887–1901.e18.

44. Cayouette, M., and Raff, M. (2002). Asymmetric segregation of Numb: a mechanism for neural specification from Drosophila to mammals. Nat. Neurosci. *5*, 1265–1269.

45. Pothof, J., Verkaik, N.S., van IJcken, W., Wiemer, E.A.C., Ta, V.T.B., van der Horst, G.T.J., Jaspers, N.G.J., van Gent, D.C., Hoeijmakers, J.H.J., and Persengiev, S.P. (2009). MicroRNA-mediated gene silencing modulates the UV-induced DNA-damage response. EMBO J. *28*, 2090–2099.

46. Aman, Y., Schmauck-Medina, T., Hansen, M., Morimoto, R.I., Simon, A.K., Bjedov, I., Palikaras, K., Simonsen, A., Johansen, T., Tavernarakis, N., et al. (2021). Autophagy in healthy aging and disease. Nat Aging *1*, 634–650.

47. Horos, R., Büscher, M., Kleinendorst, R., Alleaume, A.-M., Tarafder, A.K., Schwarzl, T., Dziuba, D., Tischer, C., Zielonka, E.M., Adak, A., et al. (2019). The small non-coding vault RNA1-1 acts as a riboregulator of autophagy. Cell *176*, 1054–1067.e12.

48. Simms, C.L., Yan, L.L., and Zaher, H.S. (2017). Ribosome collision is critical for quality control during no-go decay. Mol. Cell *68*, 361–373.e5.

49. Wolin, S.L., and Maquat, L.E. (2019). Cellular RNA surveillance in health and disease. Science *366*, 822–827.

50. Yan, L.L., Simms, C.L., McLoughlin, F., Vierstra, R.D., and Zaher, H.S. (2019). Oxidation and alkylation stresses activate ribosome-quality control. Nat. Commun. *10*, 5611.

51. Robinson, K.S., Toh, G.A., Rozario, P., Chua, R., Bauernfried, S., Sun, Z., Firdaus, M.J., Bayat, S., Nadkarni, R., Poh, Z.S., et al. (2022). ZAKα-driven ribotoxic stress response activates the human NLRP1 inflammasome. Science *377*, 328–335.

52. Rehwinkel, J., and Gack, M.U. (2020). RIG-I-like receptors: their regulation and roles in RNA sensing. Nat. Rev. Immunol. *20*, 537–551.

53. Dhir, A., Dhir, S., Borowski, L.S., Jimenez, L., Teitell, M., Rötig, A., Crow, Y.J., Rice, G.I., Duffy, D., Tamby, C., et al. (2018). Mitochondrial double-stranded RNA triggers antiviral signalling in humans. Nature *560*, 238–242.

54. Matkovic, R., Bernard, E., Fontanel, S., Eldin, P., Chazal, N., Hassan Hersi, D., Merits, A., Péloponèse, J.-M., Jr., and Briant, L. (2019). The Host DHX9 DExH-Box Helicase Is Recruited to Chikungunya Virus Replication Complexes for Optimal Genomic RNA Translation. J. Virol. *93*. e01764-e01718.

55. Rahman, M.M., Gutierrez-Jensen, A.D., Glenn, H.L., Abrantes, M., Moussatche, N., and McFadden, G. (2021). RNA helicase A/DHX9 forms unique cytoplasmic antiviral granules that restrict oncolytic myxoma virus replication in human cancer cells. J. Virol. *95*, e0015121.

56. Lawrence, P., and Rieder, E. (2009). Identification of RNA helicase A as a new host factor in the replication cycle of foot-and-mouth disease virus. J. Virol. *83*, 11356–11366.

57. Jefferson, M., Donaszi-Ivanov, A., Pollen, S., Dalmay, T., Saalbach, G., and Powell, P.P. (2014). Host factors that interact with the pestivirus N-terminal protease, Npro, are components of the ribonucleoprotein complex. J. Virol. *88*, 10340–10353.

58. Dickson, M.A., Hahn, W.C., Ino, Y., Ronfard, V., Wu, J.Y., Weinberg, R.A., Louis, D.N., Li, F.P., and Rheinwald, J.G. (2000). Human keratinocytes that express hTERT and also bypass a p16(INK4a)-enforced mechanism that limits life span become immortal yet retain normal growth and differentiation characteristics. Mol. Cell. Biol. *20*, 1436–1447.

59. Ibarra-Morales, D., Rauer, M., Quarato, P., Rabbani, L., Zenk, F., Schulte-Sasse, M., Cardamone, F., Gomez-Auli, A., Cecere, G., and Iovino, N. (2021). Histone variant.Z regulates zygotic genome activation. Nat. Commun. *12*, 7002.

60. Cox, J., and Mann, M. (2008). MaxQuant enables high peptide identification rates, individualized p.p.b.-range mass accuracies and proteome-wide protein quantification. Nat. Biotechnol. *26*, 1367–1372.

61. Zhang, X., Smits, A.H., van Tilburg, G.B., Ovaa, H., Huber, W., and Vermeulen, M. (2018). Proteome-wide identification of ubiquitin interactions using UbIA-MS. Nat. Protoc. *13*, 530–550.

62. Choi, M., Chang, C.-Y., Clough, T., Broudy, D., Killeen, T., MacLean, B., and Vitek, O. (2014). MSstats: an R package for statistical analysis of quantitative mass spectrometry-based proteomic experiments. Bioinformatics *30*, 2524–2526.

63. Keilhauer, E.C., Hein, M.Y., and Mann, M. (2015). Accurate protein complex retrieval by affinity enrichment mass spectrometry (AE-MS) rather than affinity purification mass spectrometry (AP-MS). Mol. Cell. Proteomics *14*, 120–135.

64. Zhu, Y., Orre, L.M., Zhou Tran, Y., Mermelekas, G., Johansson, H.J., Malyutina, A., Anders, S., and Lehtiö, J. (2020). DEqMS: A method for accurate variance estimation in differential protein expression analysis. Mol. Cell. Proteomics *19*, 1047–1057.

65. Ritchie, M.E., Phipson, B., Wu, D., Hu, Y., Law, C.W., Shi, W., and Smyth, G.K. (2015). limma powers differential expression analyses for RNA-sequencing and microarray studies. Nucleic Acids Res. *43*, e47.

66. Szklarczyk, D., Gable, A.L., Nastou, K.C., Lyon, D., Kirsch, R., Pyysalo, S., Doncheva, N.T., Legeay, M., Fang, T., Bork, P., et al. (2021). The STRING database in 2021: customizable protein-protein networks, and functional characterization of user-uploaded gene/measurement sets. Nucleic Acids Res. *49*, D605–D612.

67. Huang, D.W., Sherman, B.T., and Lempicki, R.A. (2009). Systematic and integrative analysis of large gene lists using DAVID bioinformatics resources. Nat. Protoc. *4*, 44–57.

68. Smits, J.P.H., Niehues, H., Rikken, G., van Vlijmen-Willems, I.M.J.J., van de Zande, G.W.H.J.F., Zeeuwen, P.L.J.M., Schalkwijk, J., and van den Bogaard, E.H. (2017). Immortalized N/TERT keratinocytes as an alternative cell source in 3D human epidermal models. Sci. Rep. *7*, 11838.

69. Końca, K., Lankoff, A., Banasik, A., Lisowska, H., Kuszewski, T., Góźdź, S., Koza, Z., and Wojcik, A. (2003). A cross-platform public domain PC image-analysis program for the comet assay. Mutat. Res. *534*, 15–20.

70. Bhardwaj, V., Heyne, S., Sikora, K., Rabbani, L., Rauer, M., Kilpert, F., Richter, A.S., Ryan, D.P., and Manke, T. (2019). snakePipes: facilitating flexible, scalable and integrative epigenomic analysis. Bioinformatics *35*, 4757–4759.

71. Dobin, A., Davis, C.A., Schlesinger, F., Drenkow, J., Zaleski, C., Jha, S., Batut, P., Chaisson, M., and Gingeras, T.R. (2013). STAR: ultrafast universal RNA-seq aligner. Bioinformatics *29*, 15–21.

72. Liao, Y., Smyth, G.K., and Shi, W. (2014). featureCounts: an efficient general purpose program for assigning sequence reads to genomic features. Bioinformatics *30*, 923–930.

73. Love, M.I., Huber, W., and Anders, S. (2014). Moderated estimation of fold change and dispersion for RNA-seq data with DESeq2. Genome Biol. *15*, 550.

74. Gaidatzis, D., Burger, L., Florescu, M., and Stadler, M.B. (2015). Analysis of intronic and exonic reads in RNA-seq data characterizes transcriptional and post-transcriptional regulation. Nat. Biotechnol. *33*, 722–729.

75. Ramírez, F., Ryan, D.P., Grüning, B., Bhardwaj, V., Kilpert, F., Richter, A.S., Heyne, S., Dündar, F., and Manke, T. (2016). deepTools2: a next generation web server for deep-sequencing data analysis. Nucleic Acids Res. *44*, W160–W165.

76. Wang, L., Wang, S., and Li, W. (2012). RSeQC: quality control of RNA-seq experiments. Bioinformatics *28*, 2184–2185.

77. Ge, S.X., Jung, D., and Yao, R. (2020). ShinyGO: a graphical gene-set enrichment tool for animals and plants. Bioinformatics *36*, 2628–2629.

78. DePristo, M.A., Banks, E., Poplin, R., Garimella, K.V., Maguire, J.R., Hartl, C., Philippakis, A.A., del Angel, G., Rivas, M.A., Hanna, M., et al. (2011). A framework for variation discovery and genotyping using next-generation DNA sequencing data. Nat. Genet. *43*, 491–498.

79. Van der Auwera, G.A., and O'Connor, B.D. (2020). Genomics in the Cloud: Using Docker, GATK, and WDL in Terra (O'Reilly Media).

80. McLaren, W., Gil, L., Hunt, S.E., Riat, H.S., Ritchie, G.R.S., Thormann, A., Flicek, P., and Cunningham, F. (2016). The Ensembl variant effect predictor. Genome Biol. *17*, 122.

81. Roth, S.J., Heinz, S., and Benner, C. (2020). ARTDeco: automatic readthrough transcription detection. BMC Bioinformatics *21*, 214.

82. Lawrence, M., Huber, W., Pagès, H., Aboyoun, P., Carlson, M., Gentleman, R., Morgan, M.T., and Carey, V.J. (2013). Software for computing and annotating genomic ranges. PLoS Comput. Biol. *9*, e1003118.

83. Bhardwaj, V., Semplicio, G., Erdogdu, N.U., Manke, T., and Akhtar, A. (2019). MAPCap allows high-resolution detection and differential expression analysis of transcription start sites. Nat. Commun. *10*, 3219.

Please cite this article in press as: Zhou et al., RNA damage compartmentalization by DHX9 stress granules, Cell (2024), https://doi.org/10.1016/j.cell.2024.02.028

CellPress
OPEN ACCESS

STAR★METHODS

KEY RESOURCES TABLE

REAGENT or RESOURCE	SOURCE	IDENTIFIER
Antibodies		
Anti-human DHX9	abcam	ab26271
Anti-human G3BP1	Santa Cruz	sc-365338
Anti-human G3BP1	GeneTex	GTX112191
Anti-dsRNA(J2 antibody)	Scicons	10010200
Anti-Flag	Sigma	F7425
Anti-human HNRNPM	Santa Cruz	sc-20002
Anti-human Nup153	abcam	ab24700
Anti-human γH2AX	abcam	ab26350
Anti-human TDP43	Thermo Fisher	A303-223A-T
Anti-dsDNA	abcam	ab27156
Anti puromycin	Merck	MABE343
Anti-human HNRNPA0	Thermo Fisher	10848-1-ap
Anti-human HNRNPA1	Thermo Fisher	11176-1-ap
Anti-human HNRNPA3	Thermo Fisher	25142-1-ap
Anti-human MATR3	Thermo Fisher	12202-1-ap
Anti-human LMNB1	Santa Cruz	sc-6216
Anti-human H3	Active Motif	39763
Anti-human pol2-S5p	abcam	ab5131
Anti-p62	GeneTex	GTX629890
Anti-DNA/RNA oxidative damage	NOVUS	NB110-96878
anti-6-4PP	Cosmo Bio LTD	CAC-NM-DND-002
anti-CPD (Thymine dimer)	Merck	T1192
anti-eIF2a	Cell Signaling	9722
anti-p-eIF2a(Ser51)	Cell Signaling	9721
anti-HuR	Santa Cruz	sc-5261
anti-PKR	abcam	ab184257
anti-p-PKR(Thr446)	abcam	ab32036
anti-VCP	Proteintech	60316
anti-P65	Cell Signaling	8242
anti-caspase3(cleaved)	Promega	G7481
anti-CAPRIN1	Thermo Fisher	16814144
anti-PABPC1	Sigma	HPA067156
anti-TIA1	Sigma	HPA056961
anti-DDX20	Thermo Fisher	11324
anti-DDX5	Cell Signaling	9877T
anti-EIF3η	Santa Cruz	sc-137214
anti-DDX17	Santa Cruz	sc-398168
Chemicals, peptides, and recombinant proteins		
Arsenite	Sigma-Aldrich	S7400
MG132	Sigma-Aldrich	M7449
Camptothecin	Sigma-Aldrich	C9911
Doxorubicin	Sigma-Aldrich	D1515
Etoposide	Sigma-Aldrich	E1383

(*Continued on next page*)

Please cite this article in press as: Zhou et al., RNA damage compartmentalization by DHX9 stress granules, Cell (2024), https://doi.org/10.1016/j.cell.2024.02.028

Continued

REAGENT or RESOURCE	SOURCE	IDENTIFIER
7,12-Dimethylbenz[a]anthracene	Sigma-Aldrich	D3254
Methyl methanesulfonate	Sigma-Aldrich	129925
4-Nitroquinoline N-oxide	Sigma-Aldrich	N8141
polIII inhibitor	Sigma-Aldrich	577784-91-9
N-Acetyl-L-cysteine	Sigma-Aldrich	A7250
4-Thiouridine	Sigma-Aldrich	T4509
Thymidine	Sigma-Aldrich	T9250
flavopiridol	Santa Cruz	sc-202157
CX-5461(polI inhibitor)	MedChemExpress	HY-13323
Poly(I:C)	InvivoGen	tlrl-pic
Pladienolide B	Cayman Chemical	16538
Critical commercial assays		
The Comet Assay Kit	abcam	ab238544
Promega GoScript Reverse Transcription System	Promega	A5001
the Oligo Clean & Concentrator Kits	Zymo Research	D4060
HiScribe™ T7 High Yield RNA Synthesis Kit	NEB research	E2040
The MEGAclear™ Transcription Clean-Up Kit	Thermo Fisher	AM1908
ViewRNA™ Cell Plus Assay Kit	Thermo Fisher	88-19000-99
Experimental models: Cell lines		
HeLa	This paper	N/A
HEK293T	This paper	N/A
N/TERT-1	Dickson et al.[58]	N/A
DHX9-eGFP; G3BP1-mCherry HeLa	This paper	N/A
DHX9-AID; Myc-Tir1 HeLa	This paper	N/A
A431	This paper	N/A
HaCAT	Christoph M.Schempp lab	N/A
G3BP1 KO HeLa	This paper	N/A
G3BP1 KO; G3BP2-AID; Myc-Tir1 HeLa	This paper	N/A
Oligonucleotides		
DNA oligos	Table S3	N/A

RESOURCE AVAILABILITY

Lead contact

Further information and requests for resources and reagents should be directed to and will be fulfilled by the lead contact, Asifa Akhtar (akhtar@ie-freiburg.mpg.de).

Materials availability

All unique materials will be available upon request to the lead contact.

Data and code availability

All deep sequencing data from this study are publicly available in the Gene Expression Omnibus database (GEO: GSE218180). Previously published HNRNPA1, NONO, TDP43, FUS, HNRNPM and EIF3G eCLIP data were obtained from the published ENCODE Project. Mass spectrometry data have been deposited to the ProteomeXchange Consortium via the MassIVE partner repository with the dataset identifiers MassIVE MSV000090634 and PXD037887.

Code used in the study is available at GitHub: https://github.com/FerallOut/Yilong_SG_Illumina_totRNAhu

Any additional information required to reanalyze the data reported in this work paper is available from the lead contact upon request.

Please cite this article in press as: Zhou et al., RNA damage compartmentalization by DHX9 stress granules, Cell (2024), https://doi.org/10.1016/j.cell.2024.02.028

CellPress
OPEN ACCESS

EXPERIMENTAL MODEL AND STUDY PARTICIPANT DETAILS

Cell culture

HeLa, HEK293T, HaCAT and A431 cells were maintained with DMEM, high glucose Glutamax (Thermo Fisher, 10569010) and 10% FBS. N/TERT-1 cells were a gift from Jim Rheinwald.[58] N/TERT-1 were maintained with Keratinocyte serum-free medium (Thermo Fisher Scientific catalogue no. 17005042) supplemented with human recombinant epidermal growth factor (rEGF) and bovine pituitary extract (BPE) according to the manufacturer's protocol.

Generation of endogenous tagged cell lines

CRISPR-Cas9 facilitated endogenous eGFP, mCherry, AID-P2A-BlasticindinR tagging of human DHX9, and eGFP and mCherry tagging of human G3BP1 were performed in HeLa cells. Primers to generate template and sgRNA carrying pX459 are listed in Table S3. The repair template was co-transfected in a 3:1 ratio with SpCas9 (pX459, Addgene no. 62988) carrying the guide RNA target DHX9 or G3BP1 gene locus by Lipofectamine™ 2000 or 3000 (Thermo Fisher, 11668027 and L3000001) in 6 well plates. Cells were selected for 3 days with 1 μg/ml puromycin starting 48 h after transfection. Cells were then replated in 10 cm dishes for another week. For AID-P2A-BlasticindinR tagged DHX9 cells, 1 μg/ml blasticidin was added. Single-cell sorting into 96-well plates was carried out by gating for the cells with the strongest GFP or mCherry signals for eGFP and mCherry tagging cells. No gating was carried out for AID-tagged cells. Colonies were expanded and screened for homozygously tagged DHX9 or G3BP1 alleles using genomic DNA PCR first followed by western blot confirmation. The DHX9-eGFP; G3BP1-mCherry HeLa cell line was generated by creating G3BP1-mCherry HeLa first and then tagging DHX9 with eGFP. The *DHX9-AID; Myc-Tir1* HeLa cell line was generated by creating *DHX9-AID* HeLa first followed by lentiviral expression of Myc-Tir1 and cultured with blasticidin and G418 selection. To rescue DHX9 expression, flag tagged DHX9 and indicated mutants were transfected into *DHX9-AID; Myc-Tir1* Hela.

For G3K cells (*G3BP1-/-; G3BP2-AID; Myc-Tir1*), CRISPR-Cas9 facilitated G3BP1 knock-out and G3BP2 AID-P2A-BlasticindinR tagging were performed in HeLa cells. Primers to generate template and sgRNA carrying pX459 are listed in Table S3. The G3BP1-KO sgRNA px459 plasmid was transfected into Hela cells by Lipofectamine™ 3000 (Thermo Fisher, 11668027 and L3000001) in 6 well plates. Cells were selected for 3 days with 1 μg/ml puromycin starting 48 h after transfection and followed by single-cell sorting into 96-well plates. Colonies were genotyped by PCR and correct ones were further validated by western blot. Endogenous AID-P2A-BlasticindinR tagging of human G3BP2 was then carried out in one of the G3BP1 fully knock-out clones. The repair template was co-transfected in a 3:1 ratio with SpCas9 (pX459, Addgene no. 62988) carrying the guide RNA target G3BP2 gene locus by Lipofectamine™ 3000 (Thermo Fisher, 11668027 and L3000001) in 6 well plates. Cells were selected for 3 days with 1 μg/ml puromycin starting 48 h after transfection. Cells were then replated in 10 cm dishes for another week with 0.5 μg/ml blasticidin. Single-cell sorting into 96-well plates was carried out then and correct clones were genome PCR and western blot validated. Myc-Tir1 was further introduced by lentiviral infection and the cells were cultured with blasticidin (0.5 μg/ml) and G418 (550 μg/ml).

All cell lines are regularly checked for the absence of mycoplasma by PCR detection kit (Jena Bioscience PP-401).

METHOD DETAILS

Stress treatments

Cells were grown to ~70% confluency then treated with sodium arsenite (As, 200 μM, 30 minutes, Sigma-Aldrich, S7400), heat shock (Hs, 43°C, 1 h), Osmosis (Os, NaCl, 0.2 M, 1 h), Poly(I:C) (10 μg/ml, transfected by Lipofectamine™ 2000, 6 h, InvivoGen tlrl-pic), MG132 (100 μM, 1 h, M7449), UVB (312nm; 500 J/m^2) and UVC (254nm; 50 J/m^2) using a cross linker (VILBER, Bio-Link) and then released 8 h unless specified otherwise, 4sU+UVA (500 μg/ml 4sU for 1 h, then treated with UVA (365nm, 500J/m^2 unless specified otherwise) and released 8 h unless specified, Camptothecin (CPT, 2 μM, 6 h, Sigma-Aldrich, C9911), Doxorubicin (Doxo, 20 μM, 6 h, Sigma-Aldrich, D1515), Etoposide (Eto, 25 μM, 6 h, Sigma-Aldrich, E1383), gamma irradiation (γIR, 1 Gy, released 6 h), Hydroxyurea (Hu, 2mM, Sigma-Aldrich, H8627, 8 h), 7,12-Dimethylbenz[a]anthracene (DMBA, 1 μg/ml, 8h, Sigma, D3254), Methyl methanesulfonate (MMS, 2 mM, 8h, Sigma, 129925), 4-Nitroquinoline N-oxide (4NQO, 5 μg/ml, 8h, Sigma, N8141), polIII inhibitor (Sigma-Aldrich, 25 μM), polII inhibitor (flavopiridol, Santa Cruz, sc-202157, 100nM), polI inhibitor (CX-5461, MedChemExpress, HY-13323, 1 μM), N-Acetyl-L-cysteine (NAC, 2mM, Sigma, A7250), Pladienolide B (PladB, 1 μM, 8 h, Cayman Chemical, 16538), OTS964 (100nM, 8 h, Cayman Chemical, 17052). Cyclophosphamide monohydrate (CPP, 10 μM, Thermo Fisher, A0444742, 8 hours), Temo, Temozolomide (Temo, 50 μM, Sigma-Aldrich, T2577, 8 hours); Methyl Nitro Nitrosoguanidine (MNNG, Sigma-Aldrich, M0252, 0.2 μM, 8 hours).

FANCI

Endogenously G3BP1-mCherry tagged or DHX9-eGFP; G3BP1-mCherry double tagged HeLa cells were used for the FANCI experiments. Cells were plated in 10 cm dishes to a 10-20% confluence with daily medium refreshing. After two days, the culturing medium was refreshed, and the cells were stressed as indicated. After the stress treatment, the culturing medium was discarded and 8 ml of fresh culturing medium (25 °C) with 1% formaldehyde was added, and the cells fixed for 15 minutes at room temperature. Then 2 M Glycine was added to a final concentration of 200 mM, and incubated for 5 minutes at room temperature to stop the fixation. The cells were washed twice with cold PBS, collected by scraping and centrifugation, and the pellets were kept on ice. Next, the pellets were

thoroughly resuspended in 2.1-2.8 ml lysis buffer B0 (50 mM HEPES pH7.5, 150 mM KCl, 1% NP40, cOmplete protease inhibitor and PhosSTOP from Roche, 1 mM DTT, RNase inhibitor (NEB, M0314L, 1:1K)). Cell lysates were then split into three to four 1.5 ml Eppendorf tubes each with 0.7 ml lysate. Lysates were incubated on ice for 20 minutes and then sonicated using the Bioruptor Plus (Diagenode) (two cycles, on 30 s, off 30 s, low energy). The lysate was kept on ice for 20 minutes, then vortexed for 5 sec and then filtered through a 40 μm Falcon cell strainer. 30 μl was reserved as the input for RNA-seq and an additional 100 μl as the input for mass spectrometry analysis. The rest was sorted using the BD FACSymphony™ S6. In contrast to normal cell sorting, the FSC and SSC thresholds were set as 200. SGs were collected in 100 μl B0 buffer supplemented with extra RNase inhibitor (1:100). Usually a 10 cm dish of cells (70% confluency) can give $3x10^5$-$4x10^5$ 4sU+UVA-induced DHX9 SGs and $1.5x10^6$ As- or Hs-induced SGs. $4x10^5$ SGs is enough to generate 7-10 ng RNA for RNA-seq. 1,200,000 SGs were collected for mass spectrometry experiments for each replicate. The SGs were collected and washed twice with B0 buffer by 2000 g, 15 minutes, swing-out centrifugation. Concentrated SGs can be checked under a microscope and snap-frozen in liquid nitrogen.

For RNA-seq, both the SGs and input were normalised to 50 μl volume with B0 buffer and digested with Proteinase K for 40 minutes at 42°C with shaking at 500 rpm. Then the samples were de-crosslinked for 40 minutes at 65°C without shaking. The RNA was cleaned using the Oligo Clean & Concentrator Kits (Zymo Research, D4060). The eluted RNA was treated with Turbo DNase for 10 minutes at 37°C and cleaned by Oligo Clean & Concentrator Kits and ready for sequencing. Illumina stranded Total RNA with Ribo-zero Plus protocol was applied for the library preparation and sequencing.

For mass spectrometry, granules were adjusted to 1% LDS, 10 mM TCEP (Sigma-Merck), and 1 mM $MgCl_2$ and treated as follows: The sample was heated at 65°C for 40 minutes, 95°C for 10 minutes, and then quickly chilled on ice before the addition of 1X benzonase (Novagen). Samples were further sonicated in a Bioruptor Plus (Diagenode) employing 10 cycles (output "high", 30 s "ON", 30 s "OFF") and chloroacetamide (Sigma-Merck) was added to 40 mM final concentration (10 minutes incubation at 37°C). Finally, samples were cleared by centrifugation in a benchtop centrifuge (Eppendorf) at 20,000 g (10°C). For SP3 magnetic beads clean-up, 7.5 μl of Sera-Mag Carboxylate-modified bead suspension (Cytiva, 20 μg/μl stock in LC-MS H_2O) was added to 163 μl of sample, and protein binding was induced by addition of neat acetonitrile to a final concentration of 71% followed by 15 minutes incubation at RT (800 rpm, Eppendorf MixMate). Beads were collected by incubation for 15 minutes at RT on an in-house constructed magnetic rack essentially as described previously[59] with the following modifications. Washing steps consisted of two washes with 544 μl 70% ethanol and one wash with 544 μl neat acetonitrile. Finally, beads were transferred to 0.5 ml low-bind tubes and briefly air-dried before reconstitution in 50 μl 50 mM ammonium bicarbonate (Honeywell). Proteolytic digestion was started with 150 ng LysC (Wako) and incubation at 37°C for 2 h (ThermoMixer, 1400 rpm). Subsequently, 600 ng sequencing grade trypsin (Promega) was admixed followed by incubation at 37°C for 12 h (ThermoMixer, 1400 rpm). Tryptic peptides were recovered by sonication (Bandelin Sonorex water bath sonicator, 2 minutes) and a two-step collection of beads consisting of a short spin (20 sec at 400 g, RT, Eppendorf benchtop centrifuge) and separation on a magnetic rack (5 minutes), which enabled the transfer of peptides to a 0.5 ml low binding tube. The beads were further extracted with 50 μl 10% acetonitrile/2% trifluoroacetic acid (ThermoMixer, 5 minutes, 25°C) and collected (magnetic rack, 5 minutes, RT). Extracted peptides were combined (100 μl volume) and reduced in vacuo to a volume of ~10 μl followed by addition of 40 μl 0.1% formic acid. Tubes were placed on a magnetic rack (5 minutes, RT) and the acidified peptides were loaded onto Evotip Pure (EV2018, Evosep) disposable tip columns that were processed according to the manufacturer's instructions with modifications outlined in the following. Evotips were first washed with 50 μl neat acetonitrile and 80% acetonitrile/0.1% formic acid, respectively (centrifugation, 1 minute, 700 g, Heraeus multifuge). Next, Evotips were conditioned with 20 μl 1-propanol (applying positive pressure with the help of a homemade syringe + adaptor). Subsequent to equilibration (0.1% formic acid, 1 minute centrifugation, 700 g) peptide samples were added on top of the Evotips, incubated for 2 minutes at RT, and loaded (1 minute centrifugation, 700 g). Last, the Evotips were washed with 50 μl 0.1% formic acid and stored at 6°C (in 0.1% formic acid) until further use.

LC-MS analysis

An Orbitrap Exploris 480 (Thermo Fisher Scientific) coupled to an Evosep One EV-1000 liquid chromatography system (Evosep) was used for all measurements. Samples were run using the 30 spd method (44 minutes gradient) on an Endurance column (EV1106, Evosep). Data was acquired in data-independent acquisition (DIA) mode with full MS resolution of 120,000 at m/z 200, AGC target 300%, mass range 350-1400 m/z, and IT of 50 ms. DIA acquisition was done with a resolution of 15,000, AGC target 3000%, and 14 m/z isolation windows with 1 m/z overlap. The precursor mass range was set to 350-1020 m/z, and a stepped normalized collision energy of 27.5±2.5 together with an IT of 22 ms was employed. General MS conditions were 2.1 kV positive ion spray voltage, 275°C ion transfer tube temperature, and RF lens voltage set to 55%.

MS data analysis

Data was analyzed using Spectronaut v16 (Biognosys), using directDIA mode with default settings. Raw files were processed using a Homo sapiens EBI reference proteome database (20,600 entries, downloaded on 03/2021) appended with an in-house curated protein contaminants catalog based on MaxQuant's contaminants list.[60]

Downstream analysis was conducted in R (R Foundation for Statistical Computing) through RStudio (RStudio: integrated Development Environment for R), using an in-house developed R package which substantially extends and complements the DEP package.[61] Briefly, proteins were summarized using MSstats dataProcess using default settings.[62] Afterward, contaminants entries were

filtered out and at least two valid quantification values in any group were required. Missing values were imputed by drawing values from a defined distribution (width 0.3, downshift 2) as described.[62,63] Statistical analysis was done using DEqMS and limma using the number of measured features and including the condition and replicate in the design matrix; comparing 4sU+UVA versus all other groups considered as common control.[64,65] Obtained p-values were corrected for multiple hypotheses by Benjamini-Hochberg, and differentially enriched proteins were classified by having an adjusted p-value ≤ 0.05.

Protein-protein interactions were carried out using only significantly changed proteins. In STRING, a "physical" network analysis was calculated (required score 0.4) and the resulting network was clustered with the Markov algorithm (MCL). Networks were generated on Cytoscape.[66] Gene Ontology enrichment analyses were done on DAVID Bioinformatics Resource using only enriched (log_2 FC > 0) significantly changed proteins and all identified proteins functioned as background.[66,67]

Puro-seq

WT HeLa and HaCAT cells were stressed as indicated and labelled with puromycin (Sigma, P4512) (10 μg/ml) for 10 minutes. Cells were immediately trypsinized and collected in cold PBS (no Mg^{2+}, no Ca^{2+}). After centrifugation, the cells were resuspended in 1 ml cold PBS (no Mg^{2+} no Ca^{2+}). 9 ml cold methanol was added and the mixture rotated at 4°C for 1 h, then centrifuged and washed once with cold PBS. The cell pellet was then resuspended in a blocking buffer (3% BSA, RNase inhibitor (NEB, M0314L, 1:500) in PBS) and incubated at 4°C for 1 h. Cells were pelleted by centrifugation and then resuspended in staining buffer (3% BSA, anti-puromycin antibody (MERCK, MABE343, 1:500), RNase inhibitor (NEB, M0314L, 1:1K)) overnight at 4°C. Cells were subsequently washed twice with cold PBS and incubated with fluorescently labelled secondary antibodies (Alexa,1:2000 in PBS) for 40 minutes. The cells were washed twice with FACS buffer (1% BSA, RNase inhibitor (NEB, M0314L, 1:500) in PBS), passed through a 70 μm cell strainer, and sorted by FACS (Beckman Coulter MoFlo XDP sorter) to collect equal number of $puro^{high}$ and $puro^{low}$ cells. Swing out centrifugation and protein low binding tubes were used to reduce cell loss. 100,000 cells were collected for RNA-seq by adding 0.5 ml Trizol (Thermo Fisher, 15596026) and extracting total RNA. Illumina stranded Total RNA with Ribo-zero Plus protocol was applied for the library preparation and sequencing.

Cell synchronization

HeLa cells were plated at 20% confluence in 6 well plates and incubated with 3 mM thymidine (Sigma-Aldrich). After 16 h, cells were released into fresh warm medium for 8 h and then incubated with 3 mM thymidine for 16 h. For early S-phase samples, these cells were treated with 4sU for 1 hour, irradiated with UVA and released into a fresh warm medium. For late S-phase samples, cells were released into a fresh warm medium for 6h and treated with 4sU for 1 hour, irradiated with UVA and released into a fresh warm medium. For G2/M-phase samples, cells were released into fresh warm medium for 6 h and incubated with 9 mM RO3306 (Alexis Biochemicals) for 4 h, then the cells were treated with 4sU for 1 hour, irradiated with UVA and released into a fresh warm medium. For G1-phase samples, cells were released into fresh medium for 10 h and subsequently incubated in 20 mM lovastatin (Santa Cruz) for 6 h, then the cells were treated with 4sU for 1 hour, irradiated with UVA and released into a fresh warm medium.

Transient transfection

HeLa cells were plated on cover glass at 60%-80% confluence in 24 well plates. Indicated plasmids were transfected into Hela cells by Lipofectamine™ 2000 (Thermo Fisher, 11668027) in antibiotic free medium for 6 hours. Cells were then treated with 4sU+UVA 18 hours later and fixed and imaged 8 hours after 4sU+UVA treatment.

RNA decay

WT HeLa cells were treated with 4sU+UVA and released for 2 h, then flavopiridol (10 μM) was added to the cells for another 4 h. Cells were collected in Trizol and Spike-In RNA (Thermo Fisher, 4456740) was added directly to the lysates according to the cell numbers. Total RNA was extracted and Illumina stranded Total RNA with Ribo-zero Plus protocol is applied for the library preparation and sequencing.

Live cell imaging

All live cell imaging experiments were performed using endogenously eGFP- and mCherry-tagged cell lines that were generated as described. Cells were cultured in DMEM-Glutamax supplemented with 10% (v/v) FCS and treated with 4sU+UVA in eight-well coverslip-bottomed dishes (ibidi GmbH cat. no. 80826). After stress, the dishes were transferred to a Tokai Hit stage incubation unit, wherein cells were maintained at 37 °C and a humidified atmosphere of 5% CO_2 throughout the experiment. Cells were imaged using a ZEISS LSM 880 confocal microscope with AIRYSCAN detector and were visualized using an air 40× or oil-immersion 63× objective. Laser power and exposure times were kept to a minimum. For live-cell RNase treatment experiments eGFP-DHX9 HeLa cells grown on coverslip-bottomed dishes were permeabilized by addition of 0.4% Triton X-100 in 1X PBS for 10 minutes at 37°C, then the buffer was carefully removed. The cells were carefully washed once with 1X PBS and RNase/DNase solution (Hoechst 33342, 1X PBS, 100 μg/ml BSA, 5 mM $MgCl_2$) containing 0.2 U/μl Turbo DNase, 200 μg/ml RNase A, 0.2U/ml RNase I or 0.2U/ml Rnase R was added to the cells. The cells were subsequently observed under the microscope for 10 minutes.

Please cite this article in press as: Zhou et al., RNA damage compartmentalization by DHX9 stress granules, Cell (2024), https://doi.org/10.1016/j.cell.2024.02.028

Immunofluorescence

Cells on coverslips were fixed with 4% methanol-free formaldehyde in PBS at room temperature for 15 minutes and permeabilized with 0.2% Triton X-100 for 5 minutes, followed by blocking with 3% BSA, 0.05% Triton X-100 in PBS for 60 minutes at RT. Cells were incubated with primary antibodies (see details in the Antibody section) diluted in PBS with 0.05% TritonX-100 and 1% BSA at 4°C for ~16 h. After washing three times with PBS (0.05% TritonX-100), the coverslips/dishes were incubated with Alexa Fluor™ 488- and Alexa Fluor™ 555 labelled secondary antibodies of the appropriate serotype (Thermo Fisher, diluted 1:1000 in PBS with 0.05% TritonX-100) for 1 h at RT. After washing three times with PBS (0.05% TritonX-100), the coverslips/dishes were mounted in Fluoromount-G™ Mounting Medium (ThermoFisher). Hoechst 33342 was added to the second washing solution for nucleus staining. Imaging was performed with a ZEISS LSM 880 confocal microscope with AIRYSCAN detector. For J2 staining, 1% methanol-free formaldehyde was used for fixation and SUPERaseIn is added to the blocking buffer. smRNA FISH was done with ViewRNA™ Cell Plus Assay Kit (ThermoFisher, 88-19000-99) according to the protocol provided.

Correlative light and electron microscopy (CLEM)

G3BP1-mCherry HeLa cells were cultured in gridded glass coverslips (ibidi, Grid-500) and treated with 4sU+UVA or arsenite. Cells were fixed in 2% PFA for 15 minutes and washed twice in PBS. Individual cells of interest were imaged with a ZEISS LSM 880 confocal microscope with AIRYSCAN detector and grid position information was recorded. Samples were then postfixed in EM fixative (4% paraformaldehyde and 2% glutaraldehyde in 0.1 M sodium cacodylate buffer, pH 7.4) for 1h at RT. Fixed samples were washed 3x in 0.1 M sodium cacodylate buffer. Contrastation (1% OsO4 in H2O; 1% Uranylacetat in H2O), dehydration (Ethanol series), and embedding in Durcupan resin were done using a PELCO BioWave® Pro+ laboratory microwave (Ted Pella Inc., Redding, CA, USA). Ultrathin sections (70nm) were prepared using a Leica UC7 ultramicrotome (Leica microsystems, Vienna), mounted on grids and contrasted using lead citrate. Sections were imaged using a transmission electron microscope operated at 120 kV (Talos L120C TEM (Thermo Scientific, Eugene, OR, USA).

Electron microscopy

WT HeLa cells were cultured in 24 well plates and stressed as indicated. Cells were fixed with glutaraldehyde 2.5% in 0.1M sodium cacodylate buffer 1h at 4° C, postfixed in osmium tetroxide 1% + potassium ferrocyanide 1% for 1h at 4° C, ethanol dehydrated, then infiltrated in a mixture of EMbed 812 (Electron Microscopy Sciences) epoxy resin and absolute ethanol 1:1, and finally embedded. Ultrathin sections were obtained with a Reichert-Yung Ultracut ultramicrotome, collected on 200 mesh copper grids, and subsequently counterstained with uranyl acetate and lead citrate. Samples were examined with a Tecnai G2 (FEI) transmission electron microscope operating at 120 kV and digital images were acquired using a Veleta (Olympus Soft Imaging Solutions) digital camera.

Protein purification

Expression and purification of DHX9 proteins was performed using a baculovirus expression system. Full-length and indicated DHX9 mutants were cloned into the 6xHis-MBP-TEV-eGFP-3C-3XFlag-pFastBac vectors wherein insertion is immediately upstream of eGFP. Recombinant baculoviruses were generated per the manufacturer's instructions (Bac-to-Bac Baculovirus Expression System, Life Technologies). Viruses were used to infect SF21 insect cells. Cells were harvested 48 h after infection by dissolving and douncing the cell pellets in HMG K150 buffer (25 mM HEPES, pH 7.6, 12.5 mM $MgCl_2$, 10% glycerol, 150 mM KCl, 0.2% NP40 (Igepal CA630) and protease inhibitor cocktail tablet (Roche)). For the purification of the recombinant proteins, FLAG-agarose beads (Anti Flag M2 Affinity Gel A2220-5ml, Sigma) were incubated with the cell extracts for 2 h and washed 3 times with HMG K150 buffer. FLAG peptides were used at 400 μg/ml (3xFlag Peptide, F4799-25 mg, Sigma) to elute the recombinant proteins. Amicon centrifugation filters (Amicon Ultra-15, 50K, VFC905024) were used to concentrate and at the same time to exchange the buffer of the purified proteins into 0.01% NP40-containing HMG K150 buffer. A fraction of the concentrated proteins was checked on an SDS-PAGE gel by Coomassie staining and protein amounts were estimated relative to a reference protein of known concentration. Proteins were snap-frozen in liquid nitrogen and stored at −80°C for later use.

Cy3-labelled RNA synthesis

roX2 exon 3 cDNA was amplified from *D. melanogaster* Schneider 2 (S2) cells with the indicated primers (Table S3) and purified using the Zymo Gel extraction Kit (Zymo Research, D4007). Forward(F) and Reverse(R) *Alu* were cloned from the 3'UTR of the human *NICN1* gene. The DNA segment was amplified with primers containing a T7 promoter in the 5' end and an EcoRI restriction site in the 3' end and inserted into pcDNA5.0 followed by linearization with EcoRI. The cDNA of *roX2* and linearized *Alu* plasmids were used to synthesize RNA *in vitro* with the HiScribe™ T7 High Yield RNA Synthesis Kit (NEB Research, E2040) plus 0.125 mM extra Cy3-UTP (Jena Bioscience, NU-821-CY3). The MEGAclear™ Transcription Clean-Up Kit (Thermo Fisher, AM1908) was used to clean up the RNA products. RNA was annealed in a buffer of 20 mM HEPES pH 7.5 and 20 mM NaCl. To normalize the Cy3 intensity between ssRNA and dsRNA, only Cy3-labelled *F-Alu* or *R-Alu* is used to generate IR-*Alu*. Annealing program: 5 minutes, 70°C, gradually cooling (0.1°C/s) to 4°C and stock at -80°C.

In vitro phase separation

Phase separation assays were typically conducted in a 5 μl volume. Proteins (100 nM unless specified otherwise) were mixed with the indicated Cy3-labelled RNA (20 nM unless specified otherwise) for 5 minutes at RT in droplet buffer (25 mM HEPES, pH 7.5, 120 mM KCl, 5% PEG-8000). Droplets were transferred to BSA-coated (10% in PBS) coverslips for observation. Droplet images were performed with a ZEISS LSM 880 confocal microscope with AIRYSCAN detector.

Protein extraction and Western blot

Protein extracts were prepared by adding 2X Roti loading buffer (ROTH, k929.1) directly to the cells followed by scraping and collection. Samples were boiled for 20 minutes. Proteins were separated using polyacrylamide gel electrophoresis in 1X MOPS buffer (Invitrogen) and transferred onto 0.2 μm polyvinylidene difluoride (PVDF) membranes (Roche) in a 1X transfer buffer (25 mM Tris-HCl pH 7.6, 192 mM glycine, 10 % methanol) for 1 h at 100 V and 4°C. Membranes were blocked in 5% milk (Biomol) in 1X PBS, 0.3% Tween-20 (PBST) for 1 h at room temperature, then incubated with primary antibodies (see Antibodies section) diluted in PBST overnight at 4°C. HRP-conjugated secondary antibodies were used at a dilution of 1:5,000 in PBST, and bands were detected using Lumi-light Western blotting substrate (Roche), and visualized using a Bio-Rad Imager.

Quantitative reverse transcription PCR (RT-qPCR)

Total RNA was extracted using the Direct-zol RNA Miniprep Plus Kit (ZymoResearch) according to the manufacturer's instructions. Promega GoScript Reverse Transcription System (Promega) was used to synthesize cDNA from total RNA according to the manufacturer's instructions. Quantitative reverse transcription PCR (RT-qPCR) was carried out on a Roche Lightcycler II using the SYBR Green Master mix (Roche) at a final volume of 10 μl. Primer sequences are provided in Table S3.

DNA Dot Blot

Total DNA from indicated cell samples were boiled in 100 °C water for 10 minutes and rapidly chilled on ice for 15 minutes. Loading position and sample label on Nitrocellulose were marked using soft pencil. Soak the membrane in sterile water for 5 minutes, then in 20× SSC for 5 minutes. Drain off the fluid and spread the membrane on several clean blotting papers, make sure that the membrane is closely attached to the blotting paper. Carefully dot 5-10μl DNA samples (100-500ng DNA) as quickly as possible as per the predecided plan. Air dry the membrane and bake at 80°C for 2 hours. After baking, membranes were incubated in a blocking buffer (5% non-fat milk in PBS) on a gentle shaker at room temperature for 2 hours. The membrane was then incubated in a blocking buffer containing mouse monoclonal antibodies against CPD or 6-4PP on a shaker at RT for 2 hours or 4 °C overnight, or directly stained with Sybr-Gold (S11494, Thermo Fisher) to detect total DNA. For blotting, wash the membrane three times (2 minutes each) using the wash buffer (0.1% Tween-20 in PBS) and incubate in a blocking buffer containing indicated horseradish peroxidase (HRP)-linked secdonary antibody at RT for 1 hour. The membrane was washed three times (10 minutes each) with the washing buffer and detected using Lumi-light Western blotting substrate (Roche), and visualized using a Bio-Rad Imager.

Human epidermal equivalent (HEE) generation

Human HEE was generated with a modified protocol as previously described.[58,68] 100ul cold Matrigel was carefully loaded in the middle of cell culture insert (3.0μM Pore size, FALCON, 353091) and gelling in 37°C for 1 hour. The N/TERT-1 cells ($0.5X10^6$) in 50μl KSM medium (Keratinocyte serum-free medium, Thermo Fisher ,17005042) were plate on top of the matrigel and let the cells settle down on the gel for 30 minutes. Then carefully fill the well with 1ml KSM and the insert with 0.5ml KSM. After 24 hours, change the medium both in the well and insert to DM (differential medium, 40% DMEM + 60% 3D medium (CnT-PR-3D, Cellntec)). Totally remove the medium inside the insert after 24 hours and keep culturing for 7 days. The medium in the wells was changed every 48 hours and any penetrated medium in the insert was removed rountingly. After indicated stresses, wash the insert once with PBS and fill the wells and insert with 4% PFA (Paraformaldehyde) for 2 hours. After fixation, wash once with PBS and carefully cut and take out the insert membrane with surgical scissors. Put the membrane (with HEE and matrigel on it) in 30% Sucrose at 4°C overnight and embedded the membrane in OCT (Optimal cutting temperature compound) and snap-freeze in liquid nitrogen. Standard 9μm frozen section was cut and loaded on a glass slide and dried at RT. Wash the sections 3 times with PBS and permeabilize with 0.2% Triton in PBS for 10 minutes, followed by 2 hours blocking (5%BSA, 1xPBS) and incubation with indicated antibodies overnight. Wash three times (15 minutes each) with a washing buffer (0.02% Triton in 1x PBS) and incubate with a blocking buffer containing indicated fluorescence conjugated secondary antibodies at RT for 1 hour. Wash three times (15 minutes each) with the washing buffer. Hoechst 33342 was added to the second washing solution for nucleus staining. The slides were then covered with Fluoromount-G™ Mounting Medium (Thermo) and cover glass and imaged under microscope.

Crystal Violet Stain

Cells in 12 well plates were washed once with PBS and fixed with 4% PFA for 15 minutes. After two times washing with PBS, add 0.5ml crystal violet staining solution (0.01% crystal violet, 1% Methonal, 1X PBS) and incubate at RT for 30 minutes. Discard the staining solution and wash with PBS five times and once with water. Air dry the plate and visualized with Bio-Rad Imager.

Please cite this article in press as: Zhou et al., RNA damage compartmentalization by DHX9 stress granules, Cell (2024), https://doi.org/10.1016/j.cell.2024.02.028

Comet assay

Comet assay was performed using the Comet Assay Kit (Abcam, ab238544) in alkaline conditions, according to the manufacturer's recommendations with minor adjustments. Briefly, 10k cells were combined with Comet Agarose in 1:5 ratio and seeded on a pre-coated comet assay slide. All the following steps were performed in dark, at 4°C, unless specified. The slide was incubated for 15 minutes, followed by a transfer to an ice-cold Lysis Buffer and incubation for 1 h. The Lysis Buffer was removed and replaced with ice-cold Alkaline Solution, and the slide was incubated for 30 minutes. Alkaline electrophoresis was run for 15' at 3V/cm, and the slide was washed three times with ice-cold water, followed by one wash with 70% ice-cold ethanol and drying at room temperature. Immediately before image acquisition, 100 ul/well of diluted Vista Green DNA Dye was added and incubated at room temperature for 15 minutes. The analysis of the comet tail moment was performed using the CASP software.[69]

Processing of RNA-seq datasets

From mapping to quantification of differential expression, the reads from RNA sequencing were analyzed using the mRNA-seq module of the snakePipes 2.5.1[70] (https://github.com/maxplanck-ie/snakepipes) using the default parameters. Briefly, the reads are trimmed using Cutadapt 2.8, and mapped to the GRCh38 genome using STAR 2.7.4a.[71] Read summarization was done with featureCounts[72] (subread 2.0.0) followed by differential analysis with DESeq2 1.26.0[72,73] and eisaR.[74] Quality control of the mRNA reads was done using FASTQC 0.11.9 (Andrews et al., 2010) and MultiQC 1.8 (Ewels et al., 2016). For quality checks specific for mRNA-seq (i.e. insert size distribution, mapping statistics, correlations, PCA and reads enrichment on various features) we used deepTools 3.3.2[75] and RSeQC 3.0.1.[76] ShinyGo 0.76.3 was used to plot gene characteristics including length and GC content.[77]

Mismatch analysis

Single nucleotide variants were called with HaplotypeCaller (GATK 4.2.6.1; Poplin et al., 2017) using best practices recommendations,[78,79] after which annotation of the SNP location and functional consequences was done using VEP 88.9.[80] For general manipulation of reads and count matrices, we used vcftools 1.2.10, bedtools 2.27.0, bedops 2.4.41, samtools 1.15.1 and various scripts were run using Rstudio 4.2.1 (Rstudio Team, 2020). Plotting was done using matplotlib 3.5.2.

DOG analysis

To quantify the readthrough transcription in each of the experimental conditions, we used the well-established ARTDeco v0.4 with default parameters.[81] Using the output from the "DoG Differential Expression" mode, and with the help of the "ggmaplot()" from the "ggpubr" library, we created MA plots showing the DE DoG genes.

RNA persistence analysis

For persistence analysis of exons and introns, we used ERCC RNA spike-in for the normalization. To analyze introns and exons separately, we summarized exon counts and gene counts with the featureCounts[72] (subread 2.0.0) option, and got intron counts by subtracting exon counts from each gene.

IR-Alu calculation

For IR-*Alu* analysis, we determined the IR-*Alu* based on the previously described method.[35] Specifically, we applied YASS (v1.14) and identified pairs of sequences with reverse-complementary to each other in each gene. For each *Alu* pair, at least 75% of the first *Alu* should be overlapped with YASS alignment and at least 75% of the second *Alu* was overlapped with the matched reverse-complementary sequence of the YASS alignment. We identified *Alu* pairs based on reverse-complementary pairs with distances shorter than 300 bp, 500 bp or 1000 bp. The annotation of *Alu*-pair-containing genes was done by GenomicFeatures,[82] with the Txdb object made of GRCh38 genome.

eCLIP data analysis

We selected proteins with both enriched in DHX9 SGs and studied in the ENCODE eCLIP project. Corresponding narrowPeak files from ENCODE (eCLIP assays in K562 cells, https://www.encodeproject.org/)[40] were downloaded. Peaks are filtered by p-value (<0.05) and annotated to genes by GenomicFeatures, with the Txdb object made of GRCh38 genome. Genes with at least one peak are recognized as indicated protein-bound RNA.

FLASH data analysis

DHX9 FLASH in HeLa cells was performed according to the previously described method[35] without any modifications. Paired-end FASTQ files were trimmed for adaptors using TrimGalore (https://github.com/FelixKrueger/TrimGalore, v 0.4.5). Possible readthroughs into the barcoded regions were removed by clipping 13 nt from the 3′ ends of first mate reads. Samples were de-multiplexed using icetea (v1.0.0, demultiplexFastq)[83] using the provided barcode information and mapped to the hg38 genome (Ensembl release 78) using STAR (v2.6.1b). For de-duplication, we considered all reads mapping to the same 5'-position and having the same random barcode as duplicates and kept only the first instance of each such alignment (using icetea—filterDuplicates). DHX9 FLASH peaks were called on alignments with PEAKachu: (https://github.com/tbischler/PEAKachu/releases/tag/0.0.1alpha2, v0.0.1alpha2) using the two replicates of the respective pulldown condition as foreground and the two replicates of the corresponding control

pull-down condition as background. BigWigs were created using deepTools (v3.1.2) bamCoverage and bamCompare. Quality control was performed using deepTools and multiQC (v1.8). For DHX9 peak density, total peaks within each gene were normalized to gene length.

QUANTIFICATION AND STATISTICAL ANALYSIS

No statistical methods were used to predetermine sample size. The experiments were not randomized and the investigators were not blinded to allocation during experiments and outcome assessment. ns: $p>0.05$, *$p<0.05$, **$p<0.01$, ***$p<0.001$, ****$p<0.0001$ unless specified otherwise.

CellPress
OPEN ACCESS

Supplemental figures

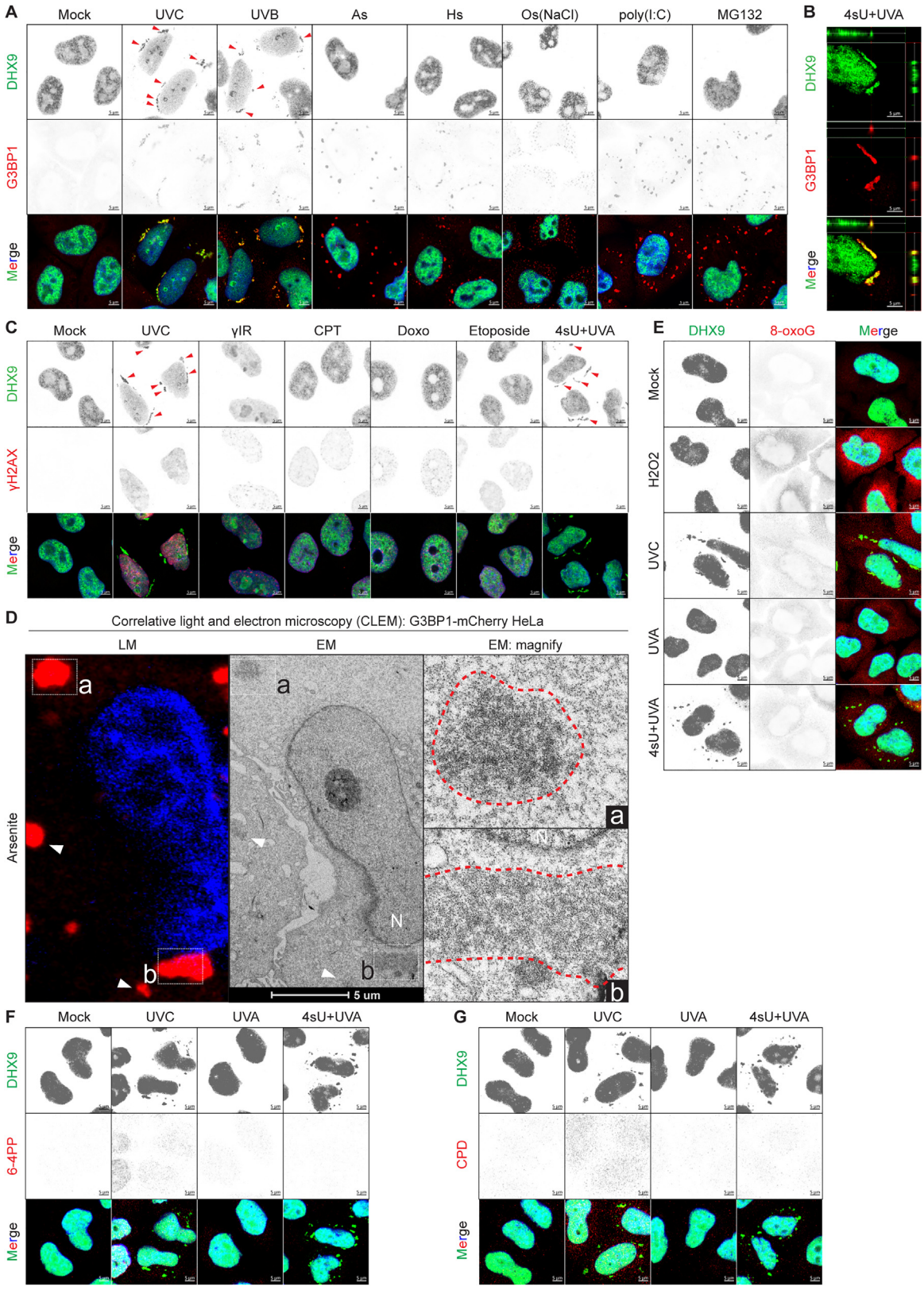

(legend on next page)

Figure S1. 4sU + UVA stress induces the assembly of DHX9 SGs, related to Figure 1

(A) Representative confocal images of DHX9 and G3BP1 staining in SGs of HeLa cells treated with the indicated stresses. As, arsenite; Hs, heat shock; Os, osmosis (0.2 M NaCl); poly(I:C), polyinosinic:polycytidylic acid. See STAR Methods for treatment conditions. Scale bars, 5 μm. Red arrows indicate DHX9 SGs.

(B) Representative 3D confocal images of DHX9 and G3BP1 signals in DHX9 SG-containing HeLa cells 8 h after 4sU + UVA stress. Scale bars, 5 μm.

(C) Representative confocal images of DHX9 and γH2AX signals in HeLa cells 8 h after different treatments. Scale bars, 5 μm. See STAR Methods for treatment conditions. Red arrows indicate DHX9 SGs.

(D) Representative confocal image and correlative electron microscopy image of G3BP1-mCherry HeLa cells 0.5 h after As treatment. White boxes mark the insets a and b, white arrows mark additional SGs located outside of the insets; red dotted lines in the insets indicate SGs; N, nucleus.

(E–G) Representative confocal images of DHX9 and 8-oxoG (E), 6-4PP (F), and CPD (G) signals in HeLa cells treated as indicated. 8-oxoG, 8-hydroxyguanine; 6-4PP, pyrimidine-pyrimidone (6-4) photoproduct; CPD, cyclobutane pyrimidine dimer. Scale bars, 5 μm.

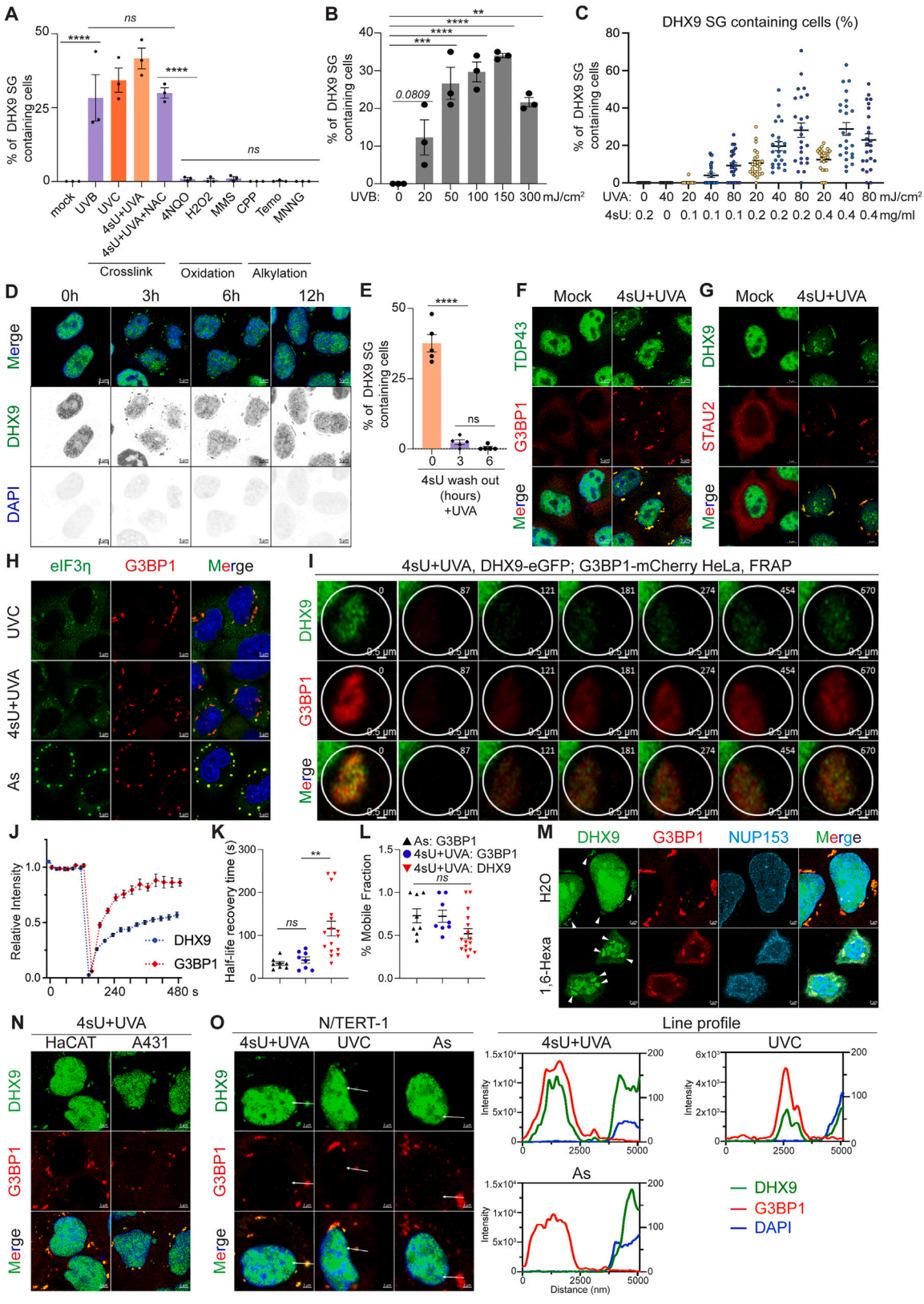

(legend on next page)

Figure S2. 4sU + UVA stress induces the assembly of DHX9 SGs, related to Figure 1

(A–C) Percentage of cells containing DHX9 SGs after the indicated treatments, mean ± SEM (n = 3 biological replicates from 3 independent experiments). N-acetyl-l-cysteine (NAC) was added immediately after UVA. CPP, cyclophosphamide monohydrate 8 h; Temo, temozolomide 8 h; MNNG, methyl nitro nitrosoguanidine 8 h. Scale bars, 5 μm. Significance was scored by ordinary one-way ANOVA. $^{**}p < 0.01$, $^{****}p < 0.0001$, ns: $p > 0.05$.

(D) Representative confocal images of DHX9 and DAPI signals in HeLa cells collected at different time points after 4sU + UVA treatment. Scale bars, 5 μm.

(E) Quantification of DHX9 SG-containing cells from HeLa cells transiently treated with 4sU for 1 h and exposed to UVA (50 mJ/cm^2) immediately afterward, 3 h later or 6 h later. Significance was scored by one-way ANOVA. $^{****}p < 0.0001$, ns: $p > 0.05$.

(F–H) Representative confocal images of the indicated proteins in HeLa cells 8 h after 4sU + UVA stress. FLAG-STAU2 is ectopically expressed in HeLa cells and detected using FLAG staining (G). Scale bars, 5 μm.

(I–L) Fluorescence recovery after photobleaching was performed on DHX9-eGFP; G3BP1-mCherry HeLa cells 8 h after 4sU + UVA or 30 min after As treatment. Representative time-lapse live-cell images (I) and quantification (J–L) of DHX9-eGFP and G3BP1-mCherry signals after photobleaching. See also Video S2. Data are shown as mean ± SEM. Significance was scored by ordinary one-way ANOVA. $^{**}p < 0.01$, ns: $p > 0.05$. Scale bars, 0.5 μm.

(M) Representative confocal images of DHX9, G3BP1, Nup153, and DAPI signals in 4sU + UVA-stressed HeLa cells recovered for 8 h and subsequently treated with 5% 1,6-hexanediol for 20 min. White arrows indicate DHX9 staining resistant to 1,6-hexanediol treatment. Scale bars, 2 μm.

(N) Representative confocal images of DHX9 and G3BP1 signals in HaCAT and A431 cells 8 h after 4sU + UVA stress. Scale bars, 5 μm.

(O) Left: representative confocal images of DHX9 and G3BP1 signals in N/TERT-1 cells treated with the indicated stresses. Right: fluorescence intensity profiles of DHX9 (green), G3BP1 (red), and DAPI (blue) across the white lines in the corresponding images. Scale bars, 2 μm.

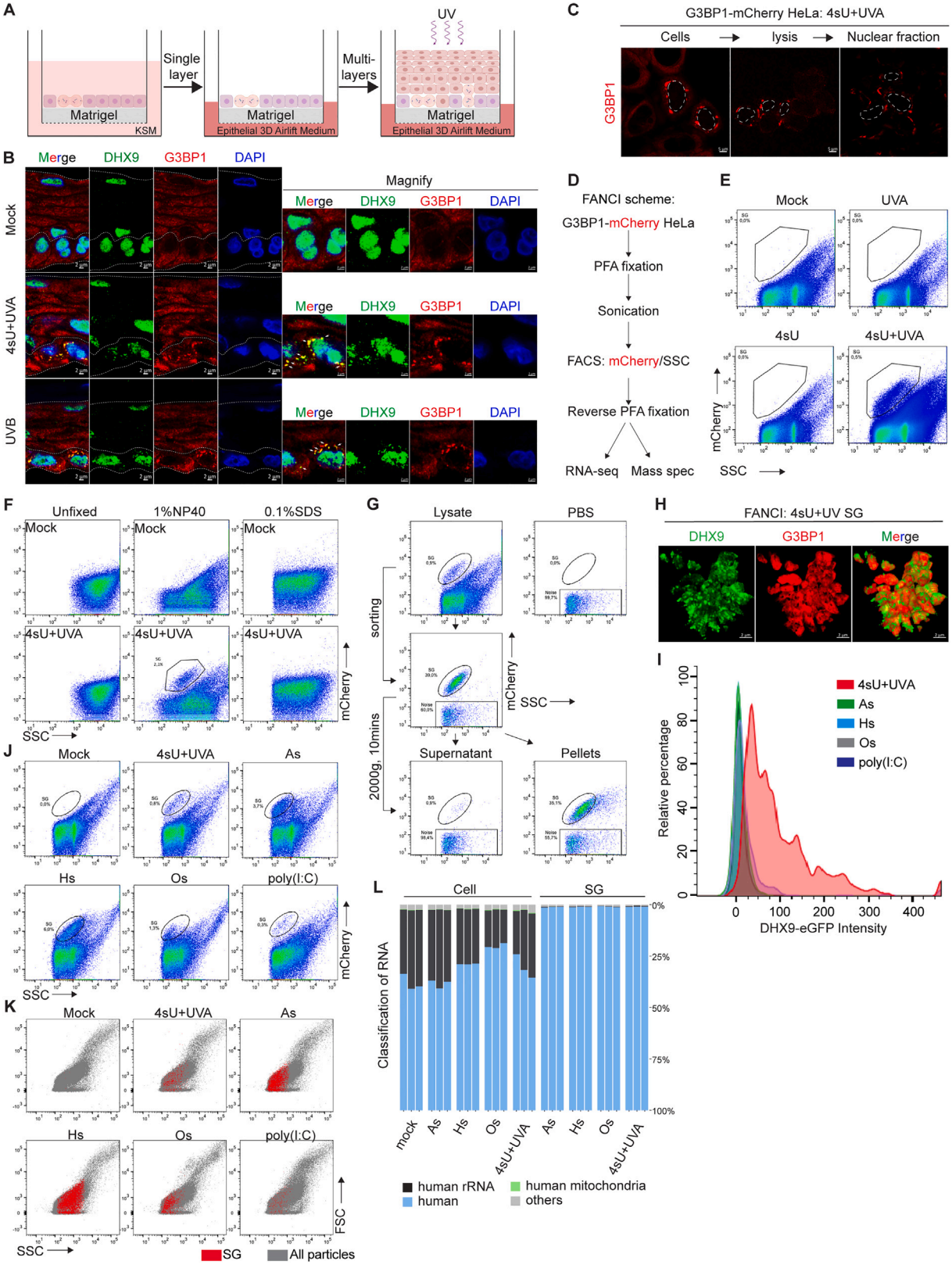

(legend on next page)

Figure S3. HEEs and the FANCI methodology, related to Figure 2

(A) Schematic overview of N/TERT keratinocyte-based HEE model culture adopted from a previous study.[68] Created with BioRender.com.

(B) Representative confocal images of DHX9 and G3BP1 signals in cryosections of HEE 8 h after treatment with 4sU + UVA (100 mJ/cm^2) or UVB (100 mJ/cm^2). White arrows indicate DHX9 SGs. Scale bars, 2 μm.

(C) Representative confocal images of G3BP1-mCherry signal in various fractions of 4sU + UVA-treated HeLa cells according to a previously published SG purification protocol.[22] White dashed line marks the nucleus. Scale bars, 5 μm.

(D) Experimental schematic of FANCI. PFA, paraformaldehyde; SSC, side scatter.

(E) Frequency of G3BP1-mCherry^{high} particles isolated using FANCI from cells treated with the indicated stresses.

(F) Optimization of FANCI protocol. FACS profiles of G3BP1-mCherry^{high} particles isolated with or without fixation and using different detergent conditions from mock or 4sU + UVA-treated HeLa cells.

(G) FACS profiles of DHX9 SGs isolated using FANCI. The granule population can easily be distinguished from the background noise generated by the flow cytometry machine, which is detectable in both lysates and PBS buffers.

(H) Representative 3D images of purified SGs from DHX9-eGFP; G3BP1-mCherry HeLa cells treated with 4sU + UVA. Scale bars, 2 μm.

(I) DHX9-eGFP intensity distribution in different SGs purified by FANCI from DHX9-eGFP; G3BP1-mCherry HeLa cells treated as indicated.

(J and K) FANCI sorting of HeLa cell lysates with the indicated stresses. The x axes represent SSC. The y axes represent G3BP1-mCherry in (J) and FSC (forward scatter) in (K).

(L) Kraken metagenomic analysis for classification of RNA isolated from the indicated samples. The category human includes all human RNA except rRNA and mtRNA.

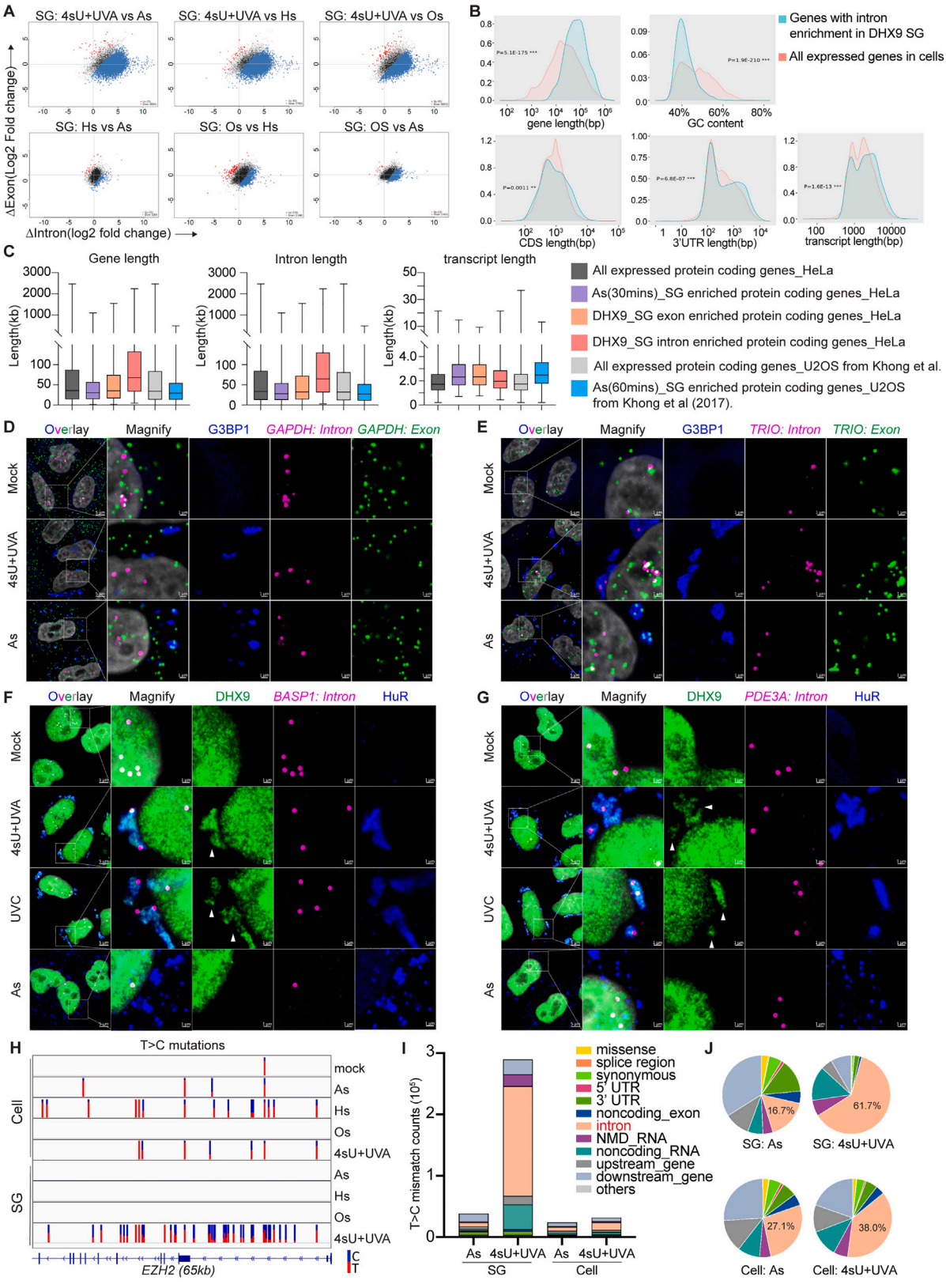

(legend on next page)

Figure S4. RNA-seq analysis of different SG subtypes, related to Figure 2

(A) Exon-intron split analysis of SG RNA by eisaR.

(B) Density plots made by using ShinyGo of the indicated gene characteristics of the genes with intron enrichment in DHX9 SGs (top 2,000, ranked by fold change) and all expressed genes in HeLa cells. The statistical significance was scored by Student's t tests.

(C) Comparison of the characteristics of the indicated protein coding genes expressed in HeLa cells, enriched in As-induced SGs, with exon enrichment in DHX9 SGs and those with intron enrichment in DHX9 SGs (top 2,000, ranked by fold change) as well as protein coding genes expressed in U2OS cells and those enriched in As-induced SGs from a previous study.[22] Center line, median; box limits, 25th to 75th percentiles; whiskers, min to max.

(D–G) Representative confocal images of indicated protein staining and smRNA FISH for the indicated gene exons and introns in HeLa cells treated as indicated. G3BP1 and HuR represent two universal SG markers. White dashed lines mark the magnified regions. White arrows in Figures S4F and S4G mark DHX9 SGs. Scale bars, 5 μm and 1 μm.

(H) IGV snapshot of T>C mismatch distribution on *EZH2* in indicated HeLa cells and purified SG RNA samples.

(I and J) Stack bar and pie chart showing the distribution of T>C mismatch in RNA from As- or 4sU + UVA-treated cells and SGs isolated from the corresponding cells.

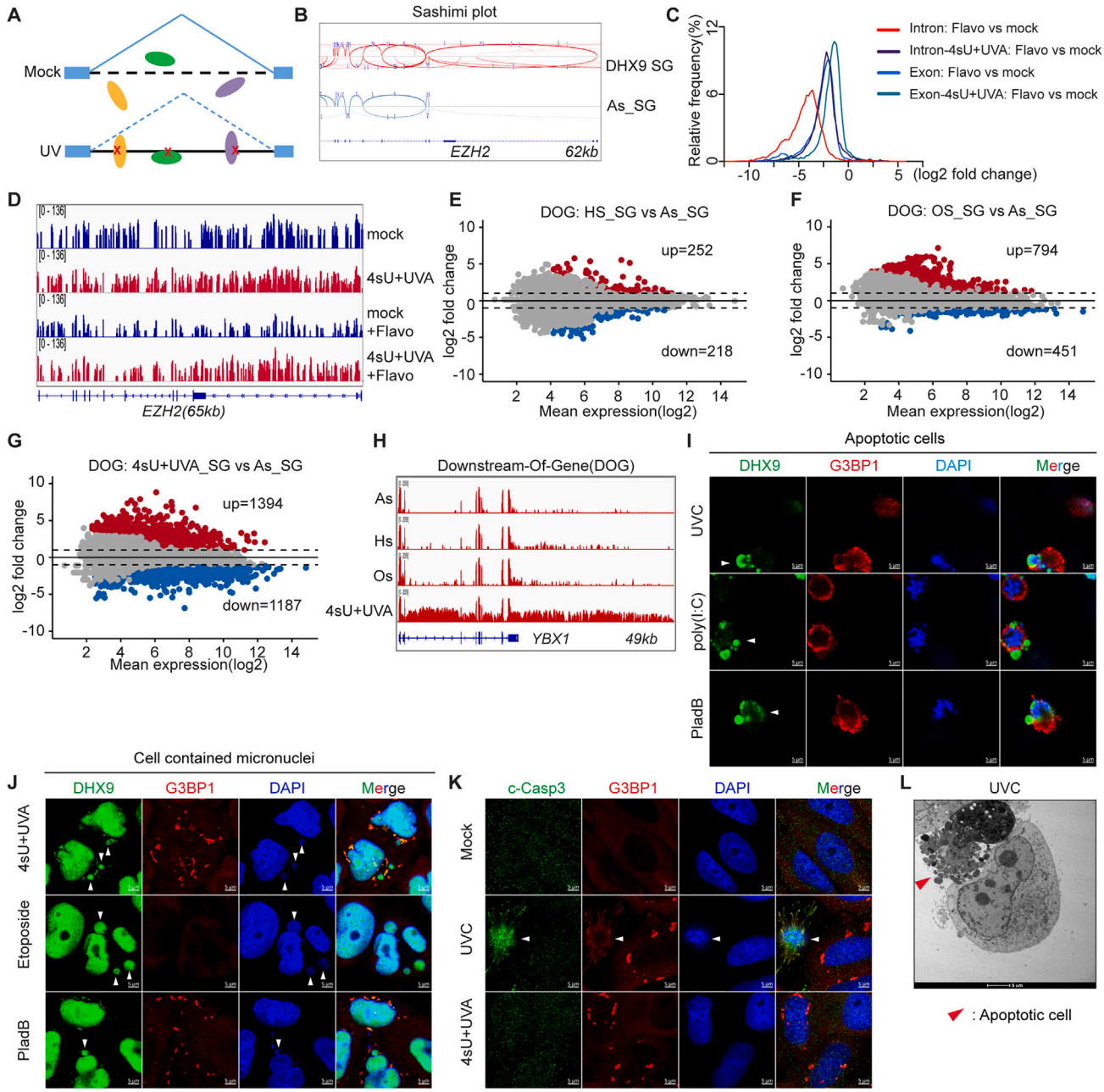

Figure S5. 4sU + UVA stress disturbs RNA processing, related to Figure 3

(A) Scheme representing the potential mode of inhibition of pre-mRNA processing by intron crosslinking damage. The failure of pre-mRNA-binding proteins to disengage from intron RNA will perturb proper splicing and degradation.

(B) Sashimi plot showed the change of splicing pattern in *EZH2*. The curved line and number on it indicate the numbers of splicing reads.

(C) Histogram of $\log_2$ fold change of all expressed intron and exon from the indicated samples.

(D) IGV snapshot of RNA-seq on gene *EZH2* from 4sU + UVA- and flavopiridol-treated samples, as indicated. A log scale is applied to the IGV tracks.

(E–G) MA plots of DOG expression comparison in indicated SG RNA samples.

(H) IGV snapshot of RNA-seq on gene *YBX1* from SG samples as indicated. A log scale is applied to the IGV tracks.

(I) Representative confocal images of DHX9 and G3BP1 signals in apoptotic HeLa cells after UVC, poly(I:C), or PladB treatments. Scale bars, 5 μm. White arrow shows an apoptotic cell.

(J) Representative confocal images of DHX9 and G3BP1 signals in micronuclei-containing HeLa cells after 4sU + UVA, etoposide, or PladB treatments. Scale bars, 5 μm. White arrows show micronuclei.

(K) Representative confocal images of cleaved-caspase-3 and G3BP1 signals in HeLa cells after 4sU + UVA or UVC treatments. Scale bars, 5 μm. White arrow shows a dead cell with c-caspase-3 staining positive.

(L) Representative electron microscopy image of apoptotic HeLa cells 8 h after UVC treatment. Red arrow shows an apoptotic cell.

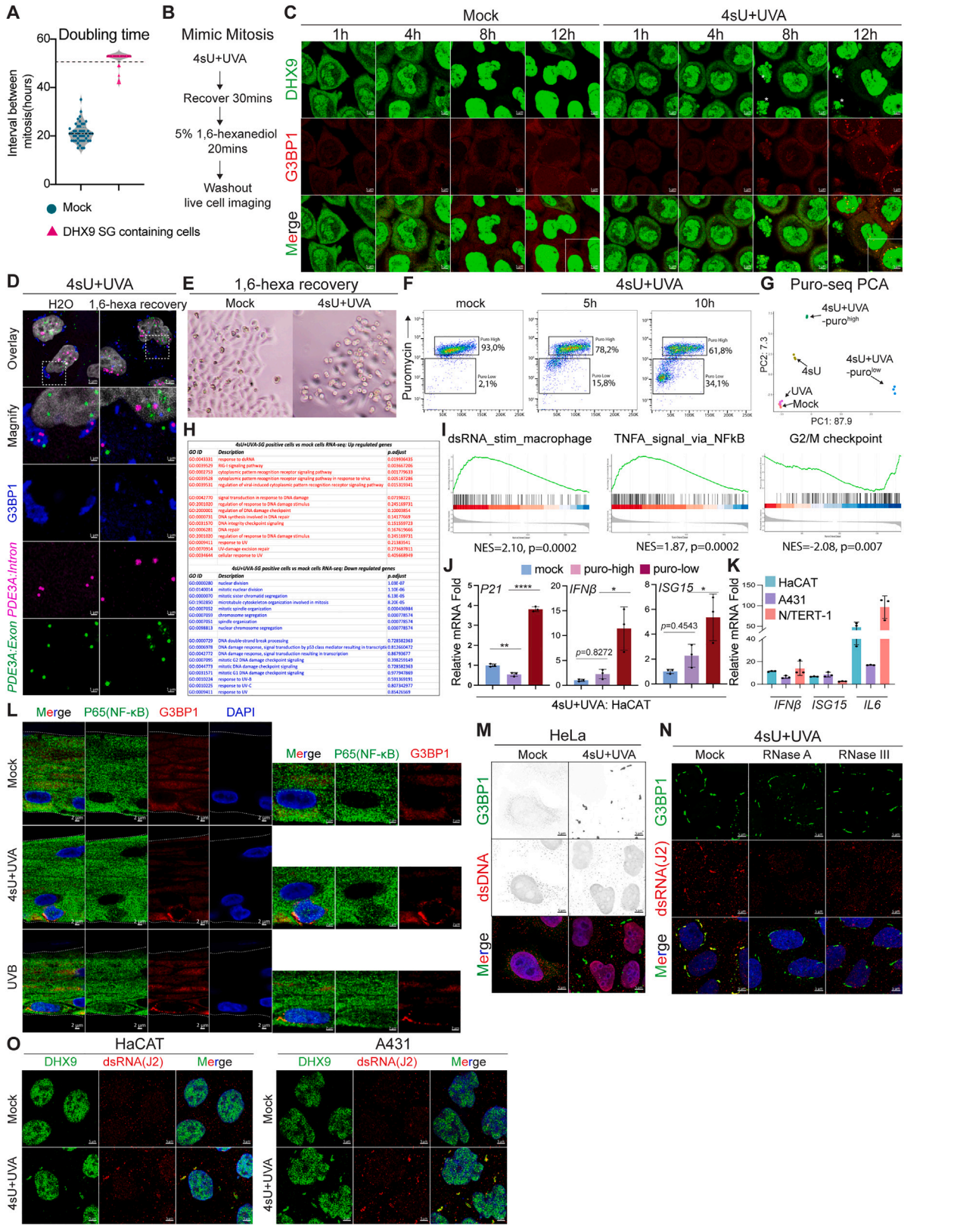

(legend on next page)

Figure S6. 4sU + UVA stress induces DHX9 SGs in daughter cells, related to Figure 4

(A) The time taken by the DHX9 SG-containing daughter cell generation to enter mitosis. The y axis represents the interval between the 1st and 2nd mitosis in hours. Dots above the dashed line indicate cells that did not undergo a second division during the observation period (=53 h) and were set as t = 53 for the purposes of data visualization. Medians are represented as dotted horizontal lines, and all points are shown within the violin plot (representative data from two independent experiments).

(B) Schematic of 1,6-hexanediol recovery experiment. HeLa cells were stressed with 4sU + UVA and after 30 min, the cells were treated with 5% 1,6-hexanediol for 20 min. Then 1,6-hexanediol was washed out, and the cells were imaged under microscope for 12 h.

(C) Representative time-lapse images of DHX9-eGFP and G3BP1-mCherry signals in HeLa cells stressed with 4sU + UVA followed by 1,6-hexanediol treatment, as shown in (B). Asterisks mark dead or dying cells. Scale bars, 5 μm.

(D) Representative confocal images of G3BP1 staining and smRNA-FISH for *PDE3A* exon and intron signals in HeLa cells 12 h after washout of 1,6-hexanediol. Cells were treated as shown in (B). Scale bars, 1 μm.

(E) Representative images of mock or 4sU + UVA-treated HeLa cells visualized 12 h after washout of 1,6-hexanediol.

(F) FACS profile of HeLa cells subjected to the 4sU + UVA treatment and pulse labeled with puromycin and collected at indicated time point.

(G) Principal-component analysis (PCA) plot of RNA-seq from puro^{low} and puro^{high} cells sorted from HeLa cells treated as indicated.

(H) Indicated Gene Ontologies and adjusted p value from Puro-seq. Also see Table S1.

(I) GSEA of differential gene categories between 4sU + UVA-treated puromycin^{low} and 4sU + UVA-treated puromycin^{high} cells.

(J) RT-qPCR quantifying changes of indicated genes in puromycin-labeled FACS-sorted HaCAT cells 12 h after 4sU + UVA stress. Data are shown as mean ± SEM. Values are normalized to the mock sample (n = 3 technical replicates from a representative experiment out of 3 independent experiments). Significance was scored by one-way ANOVA followed by a Tukey's test. *$p < 0.05$, **$p < 0.01$, ****$p < 0.0001$, ns: $p > 0.05$.

(K) RT-qPCR quantifying changes of indicated genes in indicated cells. Data are shown as mean ± SEM. Values are normalized to respective mock samples for each cell line. (n = 3 technical replicates from a representative experiment out of three independent experiments.)

(L) Representative confocal images of G3BP1 and inflammation transcription factor P65 (NF-κB) signal in the cryosection of HEE 8 h after treatment with 4sU + UVA (100 mJ/cm^2) or UVB (100 mJ/cm^2). Scale bars, 2 μm.

(M) Example confocal images of G3BP1 and dsDNA signal in HeLa cells 8 h after 4sU + UVA stress. Scale bars, 5 μm.

(N and O) Representative confocal images of G3BP1 and J2 signals in HeLa (N) and HaCAT and A431 (O) cells, treated as indicated. Fixed and permeabilized cells were treated with RNase A or III for 1 h in (N). Scale bars, 5 μm.

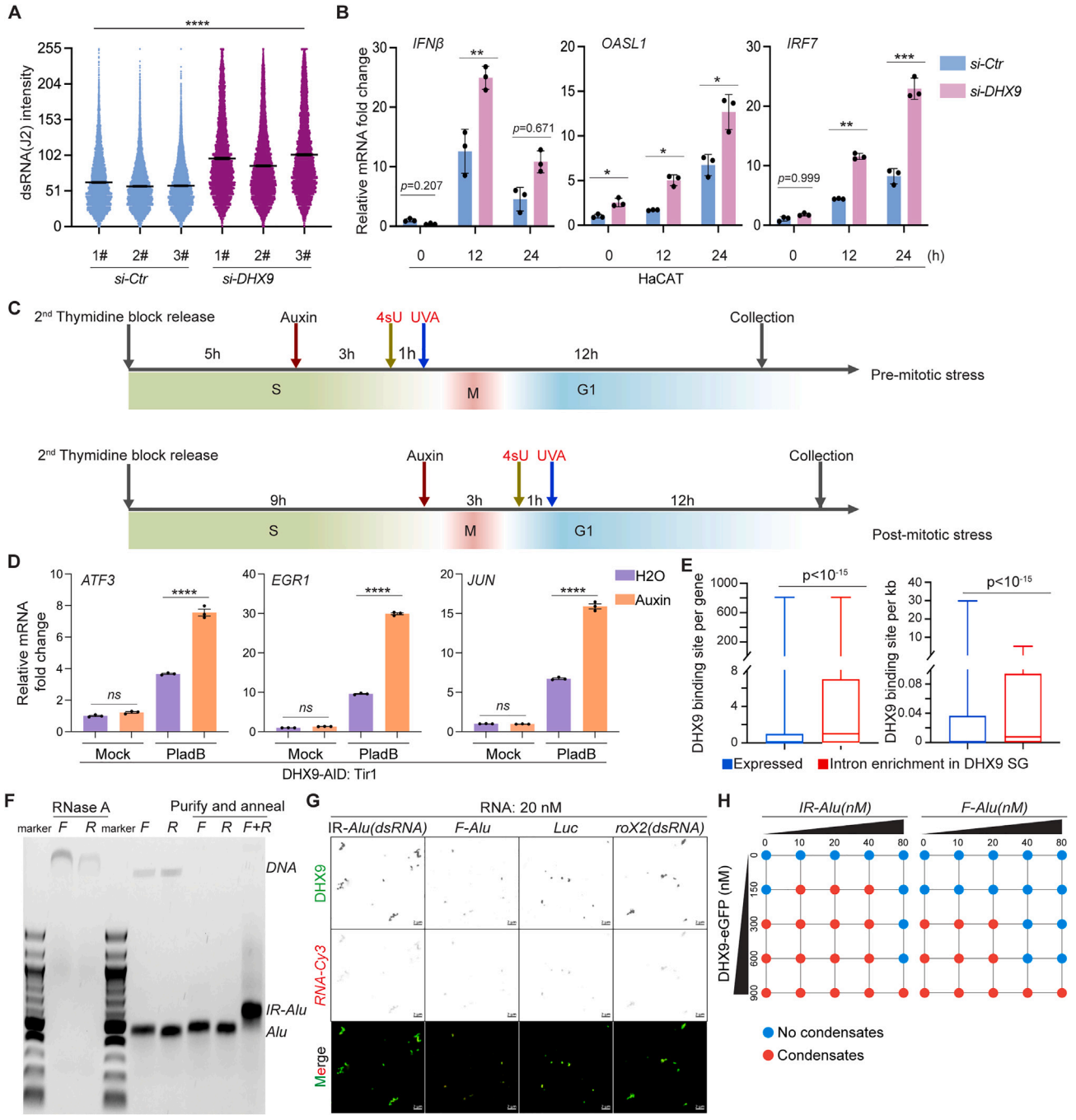

Figure S7. DHX9 modulates expression of dsRNA-related immune genes, related to Figure 5

(A) Quantification of J2 signal in SGs from control and DHX9 siRNA-treated (36 h) HeLa cells stressed with 4sU + UVA for another 8 h. Data are shown as mean ± SEM (representative data from three independent experiments). Significance was scored by non-parametric one-way ANOVA followed by a Kruskal-Wallis test. ****$p < 10^{-15}$.

(B) RT-qPCR assays quantifying changes of indicated dsRNA immune responsive genes in control and DHX9 siRNA-treated HaCAT cells stressed with 4sU + UVA. Data are shown as mean ± SEM. (n = 3 biological replicates from 3 independent experiments). Values are normalized to the si-Ctr 0-h sample. Significance was scored by two-way ANOVA followed by a Bonferroni test. *$p < 0.05$, **$p < 0.01$, ***$p < 0.001$.

(C) Experimental schematic for Figures 5D–5K. *DHX9-AID; Myc-Tir1* HeLa cells were synchronized at early S stage by double thymidine block. Pilot tests showed that the cells enter M stage about 10 h after thymidine block release, similar to wild-type HeLa cells (data not shown). The cells were treated and collected as indicated.

(legend continued on next page)

(D) RT-qPCR assays quantifying indicated gene expression changes in *DHX9-AID; Myc-Tir1* HeLa cells treated as indicated. Auxin was added together with PladB. Data are shown as mean ± SEM. (n = 3 technical replicates from a representative experiment out of 3 independent experiments). Values are normalized to the mock H_2O samples. Significance was scored by one-way ANOVA followed by a Tukey's test. ****$p < 0.0001$, ns: $p > 0.05$.

(E) DHX9-binding sites were obtained from high-throughput RNA-protein interaction data collected via the FLASH protocol and annotated as peaks summed per gene in the genome. Boxplots show the frequency of DHX9 peaks compared between genes with intron enrichment in DHX9 SGs and genes expressed in HeLa cells. The y axis depicts the numbers and density (per kb) of DHX9 peaks per gene. Center line, median; box limits, 25th to 75th percentiles; whiskers, min to max. Significance was scored by the Poisson test.

(F) SYBR Safe-stained agarose gel of *Alu* RNA produced by T7 RNA polymerase and purified and annealed as indicated.

(G and H) Representative images (G) and quantification (H) of *in vitro* phase separation assay of the indicated eGFP-tagged DHX9 proteins with Cy3-labeled ssRNA or dsRNA. Scale bars, 2 μm.

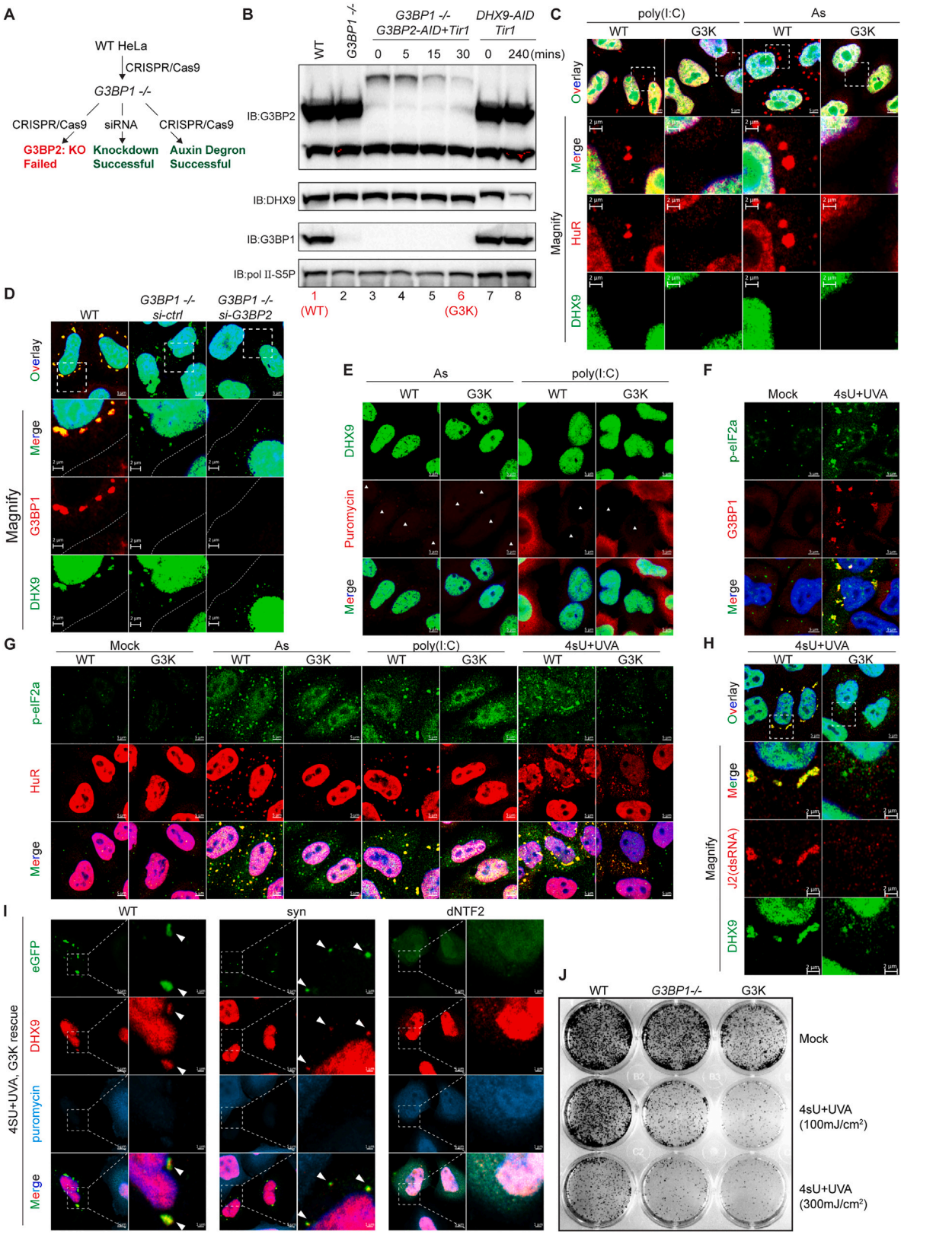

(legend on next page)

Figure S8. DHX9 SG formation is G3BP1/2 dependent, related to Figure 6

(A) Experimental schematic of G3BP1/2 depletion experiments.

(B) Immunoblot of G3BP1 and G3BP2 proteins in indicated HeLa cells. *G3BP1*$^{-/-}$*; G3BP2-AID; Myc-Tir1* HeLa cells and *DHX9-AID; Myc-Tir1* HeLa were incubated with auxin for indicated time. WT, *G3BP1*$^{-/-}$ HeLa were incubated with auxin for 30 min. RNA Pol II-S5P is used as a loading control. WT and *G3BP1*$^{-/-}$*; G3BP2-AID; Myc-Tir1* HeLa cells with auxin are treated as WT and G3K cells in indicated downstream experiments.

(C) Representative confocal images of HuR and DHX9 signals in indicated HeLa cells with As or poly(I:C) treatment. Images were saturated to display the cytosolic retention of HuR and DHX9. White dashed lines mark the magnified region. Scale bars, 5 μm and 2 μm.

(D) Representative confocal images of G3BP1 and DHX9 signals in indicated HeLa cells with 36 h of control or G3BP2 siRNA treatments and then 8 h after 4sU + UVA stresses. White dashed lines mark the magnified region. Images were saturated to display the cytosolic retention of DHX9. Scale bars, 5 μm and 2 μm.

(E) Representative confocal images of DHX9 and puromycin signals in indicated HeLa cells after As and poly(I:C) treatments and puromycin labeling. White arrows mark puromycin^{low} cells. Scale bars, 5 μm.

(F) Representative confocal images of p-eIF2a and G3BP1 signals in HeLa cells treated with 4sU + UVA. Scale bars, 5 μm.

(G) Representative confocal images of p-eIF2a and HuR signals in WT and G3K HeLa cells treated as indicated. Scale bars, 5 μm.

(H) Representative confocal images of DHX9 and J2 signals in WT and G3K HeLa cells with 4sU + UVA stress. White dashed lines mark the magnified region. Images were saturated to display the cytosolic retention of DHX9. Scale bars, 5 μm and 2 μm.

(I) eGFP-tagged WT, ΔNTF2, and synthetic G3BP1 were ectopically expressed in G3K cells for 16 h and treated with 4sU + UVA and labeled with puromycin. Representative confocal images of eGFP, DHX9, and puromycin signals are shown. White dashed lines mark the magnified region. White arrows indicate the DHX9 SGs. Scale bars, 5 μm and 1 μm.

(J) WT, *G3BP1*$^{-/-}$, and G3K HeLa cells were treated with 4sU and two different intensities of UVA, and after 3 days, cells were fixed and stained with crystal violet. 1/2 the number of indicated HeLa cells were cultured in the corresponding mock wells to prevent excessive growth.

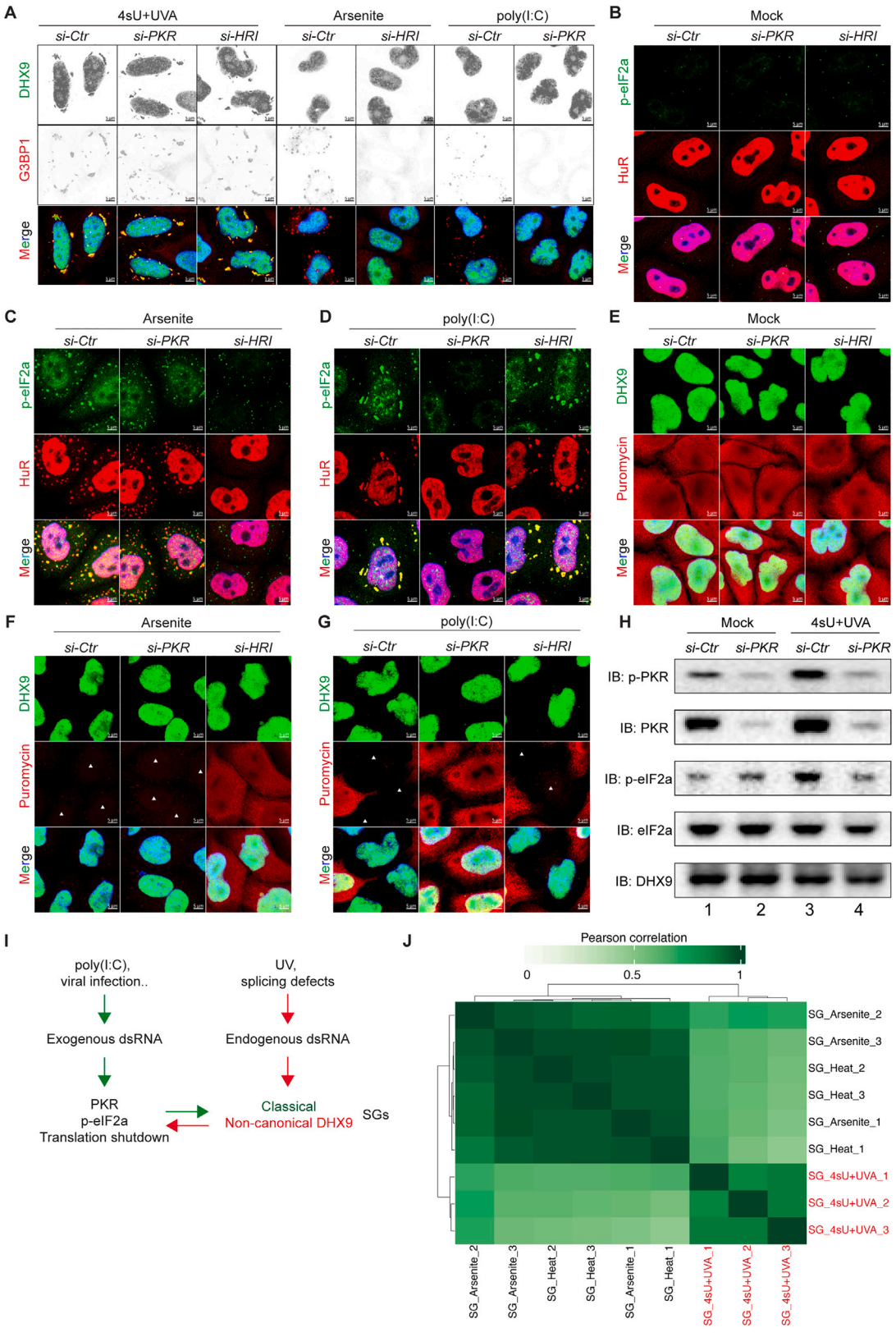

(legend on next page)

Figure S9. PKR mediates the translational arrest by 4sU + UVA, related to Figure 6

(A) Representative confocal images of DHX9 and G3BP1 signals in HeLa cells knockdown with indicated siRNA for 36 h and treated as indicated. Scale bars, 5 μm.

(B–D) Representative confocal images of p-eIF2a and HuR signals in HeLa cells knockdown with indicated siRNA for 36 h and treated as indicated. Scale bars, 5 μm.

(E–G) Representative confocal images of DHX9 and puromycin signals in HeLa cells knockdown with indicated siRNA for 36 h, treated as indicated and labeled with puromycin. White arrows mark the puromycin^{low} cells. Scale bars, 5 μm.

(H) Immunoblot of HeLa cells knocked down with indicated siRNA and treated with 4sU + UVA. DHX9 and total eIF2a are used as loading control.

(I) A summary model of the difference between virus or poly(I:C)-induced exogenous dsRNA stress response and UV-induced endogenous dsRNA stress response.

(J) Pearson correlation comparing the differentially regulated proteins between As-, Hs-, and 4sU + UVA-induced SGs.

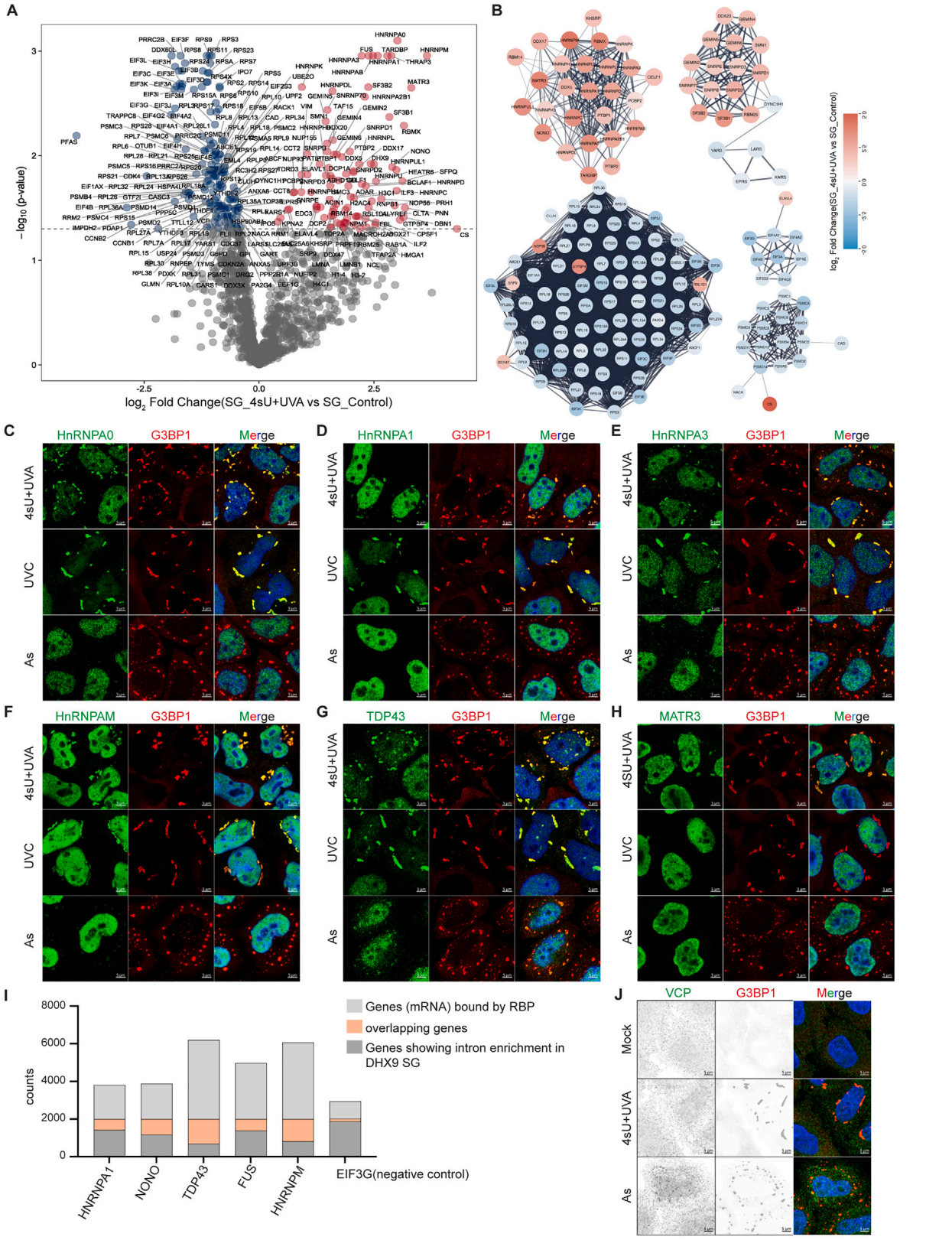

(legend on next page)

Figure S10. Comparison of the proteomes of SG subtypes, related to Figure 7

(A) Volcano plot of proteins enriched in DHX9 SGs and control SGs (As- and Hs-induced SG).

(B) STRING protein-protein interaction analysis of protein enriched in DHX9 SGs and proteins enriched in control SGs.

(C–H) Representative confocal images of G3BP1 and indicated proteins in HeLa cells subjected to 4sU + UVA, UVC, or As stresses. Scale bars, 5 μm.

(I) Identification of putative RNA-RBP interactions in DHX9 SGs. Five RBPs that are enriched in DHX9 SGs and genes showing intron enrichment (top 2,000, ranked by fold change) in DHX9 SGs were analyzed. Common genes generating mRNAs bound by the respective RBP and showed intron enrichment in DHX9 SGs are depicted in orange. Gene (mRNA) binding was defined as having >1 peak in the gene region called in the ENCODE eCLIP data. EIF3G serves as a negative control (RBP, which is not enriched in DHX9 SGs).

(J) Representative confocal images of G3BP1 and VCP signals in HeLa cells treated as indicated. Scale bars, 5 μm.